TAMPEREEN TEKNILLINEN YLIOPISTO
TAMPERE UNIVERSITY OF TECHNOLOGY

SAMU-PEKKA OJANEN

BRIGHTNESS ANALYSIS OF HIGH-POWER EDGE-EMITTING LASERS

Master of Science thesis

Examiner: D.Sc. Jukka Viheriälä
Examiner: D.Sc. Antti Härkönen
Examiners and topic approved by the Faculty Council of the Faculty of Natural Sciences
on the 20th of May 2018

ABSTRACT

SAMU-PEKKA OJANEN: Brightness analysis of high-power edge-emitting lasers
Tampere University of Technology
Master of Science thesis, 69 pages
September 2018
Master's Degree Programme in Science and Engineering
Major: Advanced Engineering Physics
Examiners: D.Sc. Jukka Viheriälä and D.Sc. Antti Härkönen
Keywords: brightness, beam quality, M squared

High-brightness lasers are the preferred sources of lights in applications that require high output power and good beam quality. One of such applications is the generation of visible light from near-infrared light through second-harmonic generation in a nonlinear crystal. Second-harmonic generation is a nonlinear process, which is highly dependent on the intensity, which means that efficient second-harmonic generation requires high power seed laser. In addition, a good beam quality is necessary to couple the laser into the nonlinear crystal efficiently.

In this thesis, ridge waveguide lasers and tapered power amplifier lasers were analyzed. The goal was to find the optimal ridge waveguide design parameters that lead to the highest brightness values, and to see if the tapered power amplifier lasers are able to achieve higher brightness compared to the ridge waveguide lasers.

Two epitaxial structures were analyzed for the ridge waveguide lasers: a symmetric structure and an asymmetric structure, emitting around 1180 nm and 1154 nm, respectively. Only the symmetric structure was analyzed for the tapered power amplifier lasers.

The output power and beam quality factors were measured and the brightness values were calculated as a function of drive current for all the laser components, and the optimum ridge waveguide design parameters leading to the highest brightness values were found for both of the epitaxial structures. The tapered laser components that were analyzed were found to have lower brightness than the ridge waveguide lasers, implying that their design should be further optimized.

TIIVISTELMÄ

SAMU-PEKKA OJANEN: Korkean tehon reuna-emittoivien laserien kirkkauden analysointi
Tampereen teknillinen yliopisto
Diplomityö, 69 sivua
syyskuu 2018
Teknis-luonnontieteellinen koulutusohjelma
Pääaine: Teknillinen fysiikka
Tarkastajat: TkT Jukka Viheriälä ja TkT Antti Härkönen
Avainsanat: kirkkaus, säteenlaatu, M toiseen

Korkean kirkkauden laserit ovat tavoiteltavia valonlähteitä sovelluksissa, joissa vaaditaan korkea ulostuloteho ja hyvä säteenlaatu. Yksi sellainen sovellus on näkyvän valon tuottaminen lähi-infrapunavalosta taajuuskahdennuksella epälineaarisessa kiteessä. Taajuuskahdennus on epälineaarinen prosessi, joka on voimakkaasti riippuvainen valon intensiteetistä, mikä tarkoittaa sitä, että tehokas taajuuskahdennus vaatii korkean tehon laserlähteen. Hyvä säteenlaatu on myös välttämätön, jotta laser saadaan kytkettyä epälineaariseen kiteeseen tehokkaasti.

Tässä lopputyössä analysoitiin harjanneaaltojohdelasereita ja taperoituja tehovahvistinlasereita. Tavoitteena oli löytää optimaaliset harjanneaaltojohteen parametrit, jolla saavutetaan suurimmat kirkkauden arvot, ja selvittää voidaanko taperoidulla vahvistinlasereilla saavuttaa suuremman kirkkauden kuin harjanneaaltojohdelasereilla.

Harjanneaaltojohdelasereiden kohdalla tarkasteltiin kahta epitaksiaalista rakennetta: symmetristä ja antisymmetristä rakennetta, joiden emissioaallonpituudet olivat noin 1180 nm ja 1154 nm. Taperoitujen vahvistinlasereiden kohdalla tarkasteltiin ainoastaan symmetristä rakennetta.

Kaikille laserkomponenteille määritettiin teho ja säteenlaatukerroin, sekä laskettiin kirkkaus virran funktiona, ja kummallekin epitaksiaaliselle rakenteelle löydettiin harjanneaaltojohteen parametrit, jotka tuottivat suurimmat kirkkauden arvot. Osoittautui, että mitattujen taperoitujen laserkomponenttien kirkkauden arvot olivat pienemmät kuin harjanneaaltojohdelaserien kirkkauden arvot, mikä viittaa siihen, että niiden rakenne vaatii optimointia.

PREFACE

This master's thesis has been done at the Optoelectronics Research Centre (ORC), Tampere University of Technology. I would like to thank Prof. Mircea Guina and Dr. Pekka Savolainen for giving me the opportunity to work and do my master's thesis at ORC. I would like to thank Ms. Anne Viherkoski and Ms. Marketta Myllymäki for helping with the paperwork and bureaucracy.

I would like to thank Dr. Jukka Viheriälä and Dr. Antti Härkönen for acting as examiners for my thesis, and for their valuable advice. I wish to thank Ms. Mervi Koskinen, and the rest of the processing team for processing the samples and performing some of the measurements that were used in this thesis. I would also like to thank Dr. Kimmo Lahtonen and Mr. Jesse Saari for performing the ALD coatings. I wish to thank my colleagues Mr. Antti Aho, Ms. Heidi Tuorila, Dr. Heikki Virtanen, and Dr. Topi Uusitalo for their helpful advice and support.

Finally, I would like to thank rest of the people working at ORC for creating such a great work environment to work in, and also my family for their love and support they have given me throughout my studies.

Tampere, 12.9.2018

Samu-Pekka Ojanen

TABLE OF CONTENTS

1. Introduction 1

2. The propagation and the beam quality of laser beams 3

2.1 Propagation of paraxial Gaussian beams 3

2.2 Beam quality factor M^2 8

2.3 Laser brightness 10

2.4 Determining the laser beam quality 12

2.4.1 Measuring the M^2 factor 12

2.4.2 The effect of spherical aberrations on the M^2 factor 14

2.4.3 Beam profiling methods 16

3. Edge-emitting semiconductor lasers 26

3.1 Basic structure of edge-emitting lasers 26

3.2 Ridge waveguide lasers 27

3.2.1 Structure of ridge waveguide lasers 27

3.2.2 Output beam divergence 28

3.2.3 Distributed Bragg reflector 30

3.3 Tapered power amplifier lasers 31

3.3.1 Structure of tapered lasers 31

3.3.2 Nonlinear effects in tapered lasers 32

3.3.3 Design of tapered lasers 33

4. Samples and characterization methods 35

4.1 Sample structures 35

4.2 Characterization methods 37

4.2.1 LI measurement 38

4.2.2 Spectrum and far field 38

4.2.3 Beam quality measurement 39

5. Results and analysis 41
5.1 Measurement results 41
5.1.1 LI curves 41
5.1.2 Spectra and emission wavelengths 44
5.1.3 Far field and numerical apertures 48
5.1.4 Beam profiles and M^2 factors 50
5.2 Brightness analysis 59
6. Summary 63
6.1 Conclusions 63
6.2 Future prospects 65
Bibliography 66

LIST OF FIGURES

2.1 Field amplitude distribution of a fundamental Gaussian beam in the transverse direction. 6

2.2 The divergence of a fundamental Gaussian beam traveling away from the beam waist. 7

2.3 Beam diameter shown as a function of distance for an ideal Gaussian beam (blue), and a transversely multimode beam (red), who both have the same divergence angle far away from the focus, but different M^2 factors. 10

2.4 A schematic figure of a typical M^2 measurement setup. 13

2.5 An example of a beam quality measurement, where the beam radius W has been measured at different distances z, and the data is fitted using Equation (2.2.5). 14

2.6 The simulated beam quality factor M^2 given as a function of the beam radius W for an ideal Gaussian beam $\left(M_0^2 = 1\right)$, when the beam is focused or collimated with a plano-convex lens with a focal length of f. In collimation, the beam enters the planar side of the lens, and, in focusing, the beam enters the convex side of the lens. 16

2.7 Schematic figure of the structure of a pixel in a CCD camera. 17

2.8 Schematic figure of the circuit of a pyroelectric element. 19

2.9 The aperture types of the scanning slit and knife-edge beam profiler. 20

2.10 The structure of a typical scanning slit or knife-edge beam profiler. . 21

2.11 The ratio of the true width and the measured width F given as a function of the ratio of the width of the slit and the beam radius X. . 22

3.1 Schematic picture of an edge-emitting laser mounted on a submount. 27

3.2 Schematic picture of the cross section of a ridge waveguide laser (not to scale). Lateral confinement of the optical field is achieved by the ridge structure, and current confinement is achieved by driving current through a thin contact formed by an insulating layer at the top of the ridge. 28

3.3 The beam radius W as a function of distance from the facet d for the fast axis (blue) and slow axis (red) of a ridge waveguide laser. Smaller output aperture leads to a broader divergence in the fast axis direction. 29

3.4 A schematic of a DBR laser. A DBR is implemented into one end of the cavity of an RWG laser to achieve single-frequency operation. . . 31

3.5 A schematic of a tapered laser. The transversely single-mode beam produced by the RWG section is broadened and amplified in the tapered section. 32

3.6 A schematic presentation of the structure and design parameters of a tapered laser. 33

4.1 (a) Symmetric, and (b) asymmetric epitaxial structures that were used in the samples. 36

4.2 A schematic of a laser diode output power measurement using an integrating sphere. 38

4.3 A schematic of a laser diode far field measurement system. 39

5.1 The output power P_{out} per facet as a function of drive current I_{RWG} for the RWG laser components with symmetric structure. 42

5.2 The output power P_{out} per facet as a function of drive current I_{RWG} for the RWG laser components with asymmetric structure. 43

5.3 The output power P_{out} as a function of drive current to the tapered section I_{taper} for the tapered DBR lasers. The drive current to the RWG section I_{RWG} was kept constant at 250 mA. 43

5.4 The spectra at two drive currents I_{RWG} for the symmetric structure RWG laser with w_{RWG} of 3.5 μm and t_{RWG} of 1300 nm. 44

5.5 The emission wavelength λ_{peak} as a function of drive current I_{RWG} for the RWG laser components with symmetric structure. 45

5.6 The spectra at two drive currents I_{RWG} for the asymmetric structure RWG laser with w_{RWG} of 4.0 μm and t_{RWG} of 1580 nm. 46

5.7 The emission wavelength λ_{peak} as a function of drive current I_{RWG} for the RWG laser components with asymmetric structure. 46

5.8 The spectra at two drive currents I_{taper} for the tapered DBR laser with DBR period of 519.9 nm. The drive current to the RWG section I_{RWG} was kept constant at 250 mA. 47

5.9 The emission wavelength λ_{peak} as a function of drive current to the tapered section I_{taper} for the tapered DBR lasers. The drive current to the RWG section I_{RWG} was kept constant at 250 mA. 47

5.10 The far field in the SA and FA directions at two drive currents I_{RWG} for the symmetric structure RWG laser with w_{RWG} of 3.5 μm and t_{RWG} of 1300 nm. 48

5.11 The far field in the SA and FA directions at two drive currents I_{RWG} for the asymmetric structure RWG laser with w_{RWG} of 4.0 μm and t_{RWG} of 1580 nm. 48

5.12 The far field in the SA and FA directions at two drive currents I_{taper} for the tapered DBR laser with DBR period of 519.9 nm. The drive current to the RWG section I_{RWG} was kept constant at 250 mA. . . . 49

5.13 The SA beam profile at beam waist, and in the far-field region at two drive currents I_{RWG} for the symmetric structure RWG laser with w_{RWG} of 3.5 μm and t_{RWG} of 1300 nm. A Gaussian beam with the same $D4\sigma$ width, and the same beam centroid as the beam at the drive current $I_{\mathrm{RWG}} = 200$ mA is included as a reference. 50

5.14 The FA beam profile at beam waist, and in the far-field region at two drive currents I_{RWG} for the symmetric structure RWG laser with w_{RWG} of 3.5 μm and t_{RWG} of 1300 nm. A Gaussian beam with the same $D4\sigma$ width, and the same beam centroid as the beam at the drive current I_{RWG} = 200 mA is included as a reference. 51

5.15 The SA beam profile at beam waist, and in the far-field region at two drive currents I_{RWG} for the asymmetric structure RWG laser with w_{RWG} of 4.0 μm and t_{RWG} of 1580 nm. A Gaussian beam with the same $D4\sigma$ width, and the same beam centroid as the beam at the drive current I_{RWG} = 200 mA is included as a reference. 52

5.16 The FA beam profile at beam waist, and in the far-field region at two drive currents I_{RWG} for the asymmetric structure RWG laser with w_{RWG} of 4.0 μm and t_{RWG} of 1580 nm. A Gaussian beam with the same $D4\sigma$ width, and the same beam centroid as the beam at the drive current I_{RWG} = 200 mA is included as a reference. 52

5.17 The SA beam profile at beam waist, and in the far-field region at two drive currents I_{taper} for the tapered DBR laser with DBR period of 519.9 nm. The drive current to the RWG section I_{RWG} was kept constant at 250 mA. A Gaussian beam with the same $D4\sigma$ width, and the same beam centroid as the beam at the drive current I_{RWG} = 4000 mA is included as a reference. 53

5.18 The FA beam profile at beam waist, and in the far-field region at two drive currents I_{taper} for the tapered DBR laser with DBR period of 519.9 nm. The drive current to the RWG section I_{RWG} was kept constant at 250 mA. A Gaussian beam with the same $D4\sigma$ width, and the same beam centroid as the beam at the drive current I_{RWG} = 4000 mA is included as a reference. 53

5.19 The beam quality factor in the SA direction M^2_{SA} as a function of drive current I_{RWG} for the RWG laser components with symmetric structure. 55

5.20 The beam quality factor in the FA direction M^2_{FA} as a function of drive current I_{RWG} for the RWG laser components with symmetric structure. 56

5.21 The beam quality factor in the SA direction M^2_{SA} as a function of drive current I_{RWG} for the RWG laser components with asymmetric structure. 57

5.22 The beam quality factor in the FA direction M^2_{FA} as a function of drive current I_{RWG} for the RWG laser components with asymmetric structure. 57

5.23 The beam quality factor in the SA direction M^2_{SA} as a function of drive current to the tapered section I_{taper} for the tapered DBR lasers. The drive current to the RWG section I_{RWG} was kept constant at 250 mA. 58

5.24 The beam quality factor in the FA direction M^2_{FA} as a function of drive current to the tapered section I_{taper} for the tapered DBR lasers. The drive current to the RWG section I_{RWG} was kept constant at 250 mA. 58

5.25 The laser brightness B as a function of drive current I_{RWG} for the RWG laser components with symmetric structure. 59

5.26 The laser brightness B as a function of drive current I_{RWG} for the RWG laser components with asymmetric structure. 60

5.27 The laser brightness B as a function of drive current to the tapered section I_{taper} for the tapered DBR lasers. The drive current to the RWG section I_{RWG} was kept constant at 250 mA. 60

LIST OF TABLES

2.1 The most common CCD sensor types, the corresponding measurable wavelength range, a typical pixel size, and the smallest beam radius that can be measured. [3] 18

4.1 The nominal ridge widths w_{RWG}, and etch depths t_{RWG} that were analyzed for the symmetric structure. 36

4.2 The nominal ridge widths w_{RWG}, and etch depths t_{RWG} that were analyzed for the asymmetric structure. 36

4.3 The nominal design parameters of the tapered laser components (see Figures 3.2 and 3.6 for definitions). 37

4.4 List of lenses that were used to collimate and focus the laser components. 40

5.1 The average divergence angles $\theta_{95\%}$ containing 95% of the output power, and the corresponding average NA values, together with the standard deviations, for all the three laser types. 49

5.2 The maximum brightness values B_{max} achieved, and the corresponding laser parameters for each of the three laser types. The error values originate from the error in the M^2 factors. 61

6.1 Summary of all the variables that lead to the maximum brightness value for the RWG lasers, together with the output power and beam quality factors. The error values originate from the error in the M^2 factors. 64

6.2 Summary of all the variables that lead to the maximum brightness value for the tapered DBR lasers, together with the output power and beam quality factors. The error values originate from the error in the M^2 factors. 64

LIST OF ABBREVIATIONS AND SYMBOLS

2D	two-dimensional
AR	anti-reflective
BCB	benzocyclobutene
CCD	charge-coupled device
CMOS	complementary metal oxide semiconductor
COD	catastrophic optical damage
CTE	coefficient of thermal expansion
DBR	distributed Bragg reflector
EEL	edge-emitting laser
EFL	effective focal length
FA	fast axis
FIR	far infrared
HR	high-reflective
LI	light output and current
MBE	molecular beam epitaxy
NA	numerical aperture
ND	neutral density
OSA	optical spectrum analyzer
QW	quantum well
RWG	ridge waveguide
SA	slow axis
SNR	signal-to-noise ratio
SHB	spatial hole burning
SHG	second-harmonic generation
UV	ultraviolet
WG	waveguide

A	area at beam focus
a	dimensionless parameter related to the fraction of the maximum peak intensity at the points between which the beam is measured
B	laser brightness
$B_{\max}$	maximum laser brightness

b	fraction of the maximum peak intensity at the points between which the beam is measured
C_4	quartic-aberration coefficient
E_0	maximum value of the field amplitude
$\mathrm{erf}(x)$	error function
F	ratio of true width and measured width
f	lens focal length
G	Gaussian distribution
I	drive current
$I(x, y, z)$	intensity distribution
k	propagation constant
L_{DBR}	length of the DBR
L_{RWG}	length of the RWG
L_{taper}	length of the tapered section
$M(z)$	measured profile in scanning slit beam profiler
M^2	beam quality factor
M_0^2	non-degraded beam quality factor
M_q^2	beam quality parameter that describes spherical aberrations
NA	numerical aperture of a lens or a laser
$\mathrm{NA}_{95\%}$	numerical aperture containing 95% of the output power
n_{eff}	effective refractive index
P	complex phase shift, output power
p	parameter describing radii of curvature of a beam with respect to the focal length of a lens
q	complex beam parameter, parameter describing lens shape
R	radius of curvature of the wavefront
r	radial distance from the propagation axis
s	slit width
t_{DBR}	etch depth of the DBR
t_{RWG}	etch depth of the ridge
u	electromagnetic field or potential
W	beam radius
W_q	critical beam radius
w	Gaussian beam radius
w_{DBR}	DBR width
w_{RWG}	ridge width
X	ratio of slit width and beam radius

x	x coordinate
y	y coordinate
z	distance
z_R	Rayleigh range or Rayleigh length
$\langle x \rangle$, $\langle y \rangle$	first-order moments in x- and y-direction
$\langle x^2 \rangle$, $\langle y^2 \rangle$	second-order moments in x- and y-direction
θ	divergence half-angle far away from the focus
θ_0	lens or laser acceptance angle
$\theta_{1/e}$	divergence half-angle of a fundamental Gaussian beam far away from the focus
$\theta_{95\%}$	divergence half-angle containing 95% of the output power
θ_{out}	output angle
θ_{taper}	opening angle of the tapered region
λ	wavelength
λ_{peak}	peak emission wavelength
σ	standard deviation
ψ	complex function describing diffraction-related effects
Ω	far field solid angle

1. INTRODUCTION

Since the discovery of laser diodes, they have been used in many applications, such as data storage, fiber-optic communication systems, and medical applications. Laser diodes have many advantages over solid-state, dye, and fiber lasers, including their compact size, long-time reliability, superior wallplug efficiency, wavelength flexibility, and lower cost per emitter. [14, p. 1–5]

In many applications it is desirable for the laser to have a high output power with a high quality Gaussian beam. These parameters can be characterized simultaneously by considering laser brightness, which takes into account the output power, beam quality, and the wavelength of the laser. In practice, it is difficult to build high-brightness laser diodes. Ridge waveguide (RWG) laser diodes have a nearly diffraction-limited beam, but they are restricted to relatively low powers due to catastrophic optical damage (COD) caused by too high intensity at the facets [30]. Broad-area laser diodes can achieve output power in the order of tens of watts [22], but usually they have a very poor beam quality, leading to a low brightness.

There are several ways to achieve high output power with improved beam quality. One way is to build a so-called tapered laser. In this kind of system, a relatively low power laser, such as an RWG laser, with a nearly diffraction-limited beam is injected into a tapered gain region, which amplifies and widens the beam towards the output facet. With an appropriate design of the tapered region, this will lead to a high output power with good beam quality. However, when the drive current is increased, the output power of the laser increases, and at some point such high output powers are reached that nonlinear effects become important, and this leads to the deterioration of the laser beam quality. When designing tapered lasers, it is important to minimize the nonlinear effects, in order to achieve high brightness values. [37]

In this thesis, laser diodes emitting at 1180 nm and 1154 nm were analyzed. In the final application, the lasers will be frequency-doubled to yellow wavelength region by

second-harmonic generation (SHG) in a nonlinear crystal. The resulting 590 nm and 577 nm lasers will be used in medical applications. Efficient coupling to the nonlinear waveguide crystal requires high beam quality, and high output power at the laser source is useful because the intensity of the frequency-doubled light is proportional to the square of the intensity of the input light [26]. In other words, the laser source must have high brightness in order to achieve good power conversion efficiency.

RWG lasers made from two types of epitaxial structures were analyzed: a symmetric structure and an asymmetric structure, with emission at 1180 nm and 1154 nm, respectively. The goal was to find the RWG parameters that lead to the highest brightness value. In addition, two tapered lasers with the symmetric epitaxial structure, and a distributed Bragg reflector (DBR) implemented to the back facet, were analyzed. The goal was to analyze their brightness, and to see if there is an improvement in the brightness compared to the RWG lasers.

2. THE PROPAGATION AND THE BEAM QUALITY OF LASER BEAMS

In order to characterize the quality of a laser beam, it is essential to understand how Gaussian beams propagate. This can then be extended to arbitrary laser beams by introducing a so-called beam quality factor into the equations. In this chapter, the propagation equation for arbitrary beams is derived, and the method for defining the beam quality factor is introduced, together with the effects of spherical aberrations. Finally, beam profiling methods are introduced.

2.1 Propagation of paraxial Gaussian beams

Gaussian-shaped beams are important because of their many important properties, such as [27]:

- The shape of a Gaussian beam does not change as it passes through diffraction-limited optical elements. Only its width changes.
- The first-order field distributions in optical resonators are usually Gaussian, provided that there are no beam distorting elements inside the cavity.
- The beam profiles in single-mode optical fibers are usually very close to a Gaussian shape.
- The propagation of an arbitrary ray can be described with the same equations that apply to ideal Gaussian beams if we introduce a so-called beam quality factor into the equations.

It is often required that lasers operate at single transverse mode, in which case they are Gaussian-shaped, because such lasers have favorable properties, such as better focusability and higher coupling efficiency to fibers, compared to multimode lasers.

To be able to design optical systems and characterize laser beams, it is important to know how the size of a Gaussian beam changes as it propagates.

Here it is assumed that the apertures are sufficiently large to avoid diffraction effects. It is also assumed that the transverse size of the beam is much larger than the wavelength, which is generally true for most laser beams.

An electromagnetic field or potential u in an uniform and isotropic medium satisfies the Helmholtz equation [16, p. 532–533]:

$$\nabla^2 u + k^2 u = 0, \tag{2.1.1}$$

where

$$k = \frac{2\pi}{\lambda} \tag{2.1.2}$$

is the propagation constant, where λ is the wavelength in the medium. A beam that propagates in the z direction is of the form [17]

$$u = \psi(x, y, z)e^{-jkz}, \tag{2.1.3}$$

where ψ is a complex function that describes the transverse intensity distribution of the beam, the expansion of the beam with propagation, and the curvature of the phase front. In other words, ψ describes the diffraction-related effects. Substituting this function into Equation (2.1.1) results in

$$\frac{\partial^2 \psi}{\partial x^2} + \frac{\partial^2 \psi}{\partial y^2} + \frac{\partial^2 \psi}{\partial z^2} - 2jk\frac{\partial \psi}{\partial z} = 0, \tag{2.1.4}$$

Assuming that ψ varies slowly with z, the second order term can be neglected:

$$\left|\frac{\partial^2 \psi}{\partial z^2}\right| \ll \left|2k\frac{\partial \psi}{\partial z}\right|, \left|\frac{\partial^2 \psi}{\partial x^2}\right|, \left|\frac{\partial^2 \psi}{\partial y^2}\right|, \tag{2.1.5}$$

and this will lead to the equation

$$\frac{\partial^2 \psi}{\partial x^2} + \frac{\partial^2 \psi}{\partial y^2} - 2jk\frac{\partial \psi}{\partial z} = 0, \tag{2.1.6}$$

which is often called the paraxial wave equation [17]. In practice, this equation applies when the propagation angle of all the plane wave components of the beam are less than 0.5 rad or 30°. If this applies, the term $\frac{\partial^2 \psi}{\partial z^2}$ is at least one order of

magnitude smaller than all the other terms in Equation (2.1.4). Beams propagating at larger angles require higher-order correction terms. [32, p. 628–630]

It can be shown that one of the solutions to the paraxial wave equation (2.1.6) is of the form [17]

$$\psi \propto \exp\left[-j\left(P + \frac{k}{2q}r^2\right)\right], \tag{2.1.7}$$

where $r^2 = x^2 + y^2$ is the radial distance from the propagation axis, $P(z)$ is a complex phase shift, which is related to the propagation of the beam, and $q(z)$ is a complex beam parameter, which describes the curvature of the phase front and the shape of the beam with respect to r. A beam with this kind of shape is also known as the fundamental Gaussian mode [17]. Substituting this solution to the paraxial wave equation (2.1.6) will lead to a relation between the beam parameter in the input and output plane, q_1 and q_2, respectively:

$$q_2 = q_1 + z. \tag{2.1.8}$$

Let us define two real terms R and w, such that

$$\frac{1}{q} = \frac{1}{R} - j\frac{\lambda}{\pi w^2}. \tag{2.1.9}$$

By substituting this definition to Equation (2.1.7), it can be seen that R is the radius of curvature of the wavefront, and w is the beam radius, which corresponds to the transverse distance at which the field amplitude is $1/e$ of its maximum value. Figure 2.1 shows an example of the field amplitude distribution of a fundamental Gaussian beam, where E_0 is the maximum value of the field amplitude, and $2w$ is the diameter of the beam.

The Gaussian beam radius w reaches its minimum value w_0 at the beam waist where R approaches infinity, which corresponds to a plane wave. The beam parameter at beam waist is

$$q_0 = j\frac{\pi w_0^2}{\lambda}. \tag{2.1.10}$$

If the beam propagation is measured from the waist to some arbitrary distance z, the beam parameter can be written as

$$q = q_0 + z = j\frac{\pi w_0^2}{\lambda} + z. \tag{2.1.11}$$

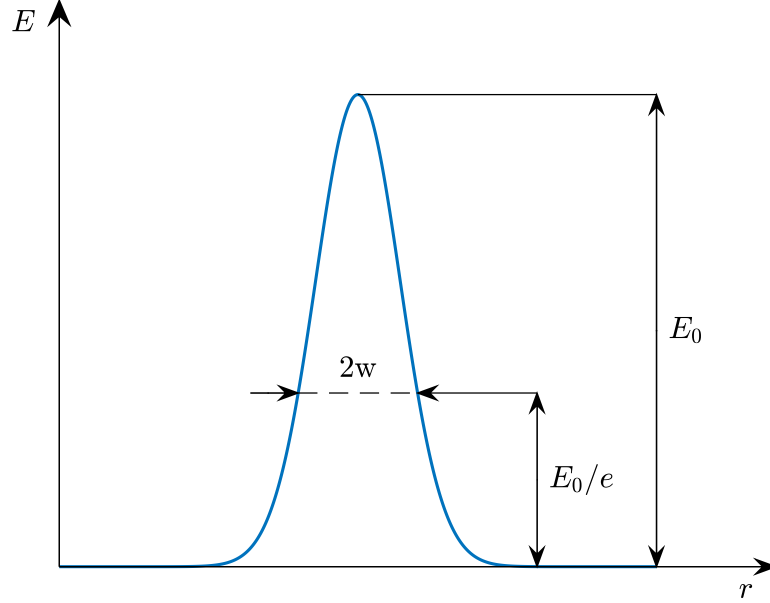

Figure 2.1 *Field amplitude distribution of a fundamental Gaussian beam in the transverse direction.*

Substituting this into Equation (2.1.9), and equating the real and imaginary parts, leads to an expression for the beam radius $w(z)$ and the curvature of the wavefront $R(z)$ as a function of z:

$$w(z) = w_0 \sqrt{1 + \left(\frac{\lambda z}{\pi w_0^2}\right)^2}, \tag{2.1.12}$$

$$R(z) = z \left[1 + \left(\frac{\pi w_0^2}{\lambda z}\right)^2\right]. \tag{2.1.13}$$

The beam radius $w(z)$ forms a hyperbola, with an asymptote angle

$$\theta_{1/e} = \frac{\lambda}{\pi w_0}. \tag{2.1.14}$$

This is the divergence half-angle far away from the focus for a fundamental Gaussian beam [17], which contains 68% of the energy of the beam. The divergence of a fundamental Gaussian beam from the beam waist is illustrated in Figure 2.2.

The distance from the beam waist where the beam radius is increased by a factor of $\sqrt{2}$, or before the area of a circular beam is doubled, is referred to as Rayleigh range

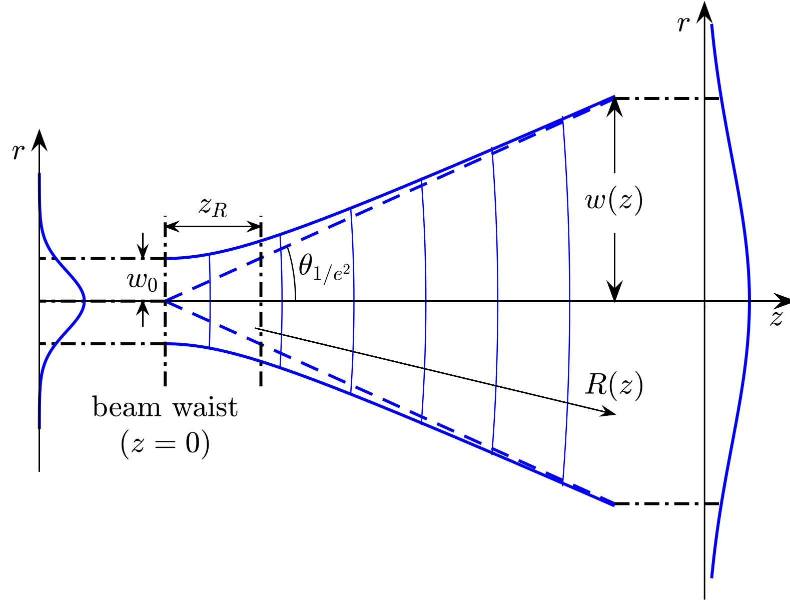

Figure 2.2 *The divergence of a fundamental Gaussian beam traveling away from the beam waist.*

or Rayleigh length, and is defined as [32, p. 668–669]

$$z_R = \frac{\pi w_0^2}{\lambda}, \tag{2.1.15}$$

which is the imaginary part of the complex beam parameter q. Rayleigh range is an approximate dividing line between the near-field and far-field regions, and it can also be thought as the depth of focus of a beam, in the sense that when a beam propagates away from the beam waist, it starts to diverge rapidly at distance z_R from the waist. By using z_R, $w(z)$ and $R(z)$ can be written in a more simple form:

$$w(z) = w_0\sqrt{1 + \left(\frac{z}{z_R}\right)^2}, \tag{2.1.16}$$

$$R(z) = z + \frac{z_R^2}{z}. \tag{2.1.17}$$

Only the fundamental mode of the paraxial wave equation was described here. The paraxial wave equation has also higher-order solutions: Hermite-Gaussian modes in Cartesian coordinates, and Laguerre-Gaussian modes in cylindrical coordinates. Together these solutions form a complete orthogonal set of functions known as the modes of propagation. Any arbitrary monochromatic beam can be expressed as a

linear combination of these functions. [17]

2.2 Beam quality factor M^2

The equations for the beam radius $w(z)$ and the radius of curvature of the wavefront $R(z)$, derived in the previous section, only apply to laser beams that operate in the fundamental mode. However, laser beams are often not fully transversely single-mode, but instead they may be distorted or contain higher-order propagation modes. By utilizing Equations (2.1.16) and (2.1.17), a more general formalism can be derived, that applies to any arbitrary beam, which may be non-Gaussian, elliptic, and astigmatic.

Let us define the beam radius of an arbitrary beam, such that the beam radii in x- and y-direction are [35]

$$W_x(z) = 2\sigma_x \equiv 2\sqrt{\langle x^2\rangle} = 2\sqrt{\frac{\iint (x - \langle x\rangle)^2 I(x, y, z)\ dx\, dy}{\iint I(x, y, z)\ dx\, dy}}, \tag{2.2.1}$$

$$W_y(z) = 2\sigma_y \equiv 2\sqrt{\langle y^2\rangle} = 2\sqrt{\frac{\iint (y - \langle y\rangle)^2 I(x, y, z)\ dx\, dy}{\iint I(x, y, z)\ dx\, dy}}, \tag{2.2.2}$$

where σ_x and σ_y are the standard deviations in x- and y-direction, $\langle x^2\rangle$ ja $\langle y^2\rangle$ are the second-order moments in x- and y-direction, $I(x, y, z)$ is the intensity distribution of the beam, and

$$\langle x\rangle(z) = \frac{\iint xI(x, y, z)\ dx\, dy}{\iint I(x, y, z)\ dx\, dy} \tag{2.2.3}$$

and

$$\langle y\rangle(z) = \frac{\iint yI(x, y, z)\ dx\, dy}{\iint I(x, y, z)\ dx\, dy} \tag{2.2.4}$$

are the first-order moments in x- and y-direction, which define the centroid of the beam. This method is known as the $D4\sigma$ method, because the obtained beam diameters are four times the standard deviations defined in Equations (2.2.1) and (2.2.2). By defining the beam radii using the $D4\sigma$ method, it can be shown that the beam radius of an arbitrary beam in x- and y-direction follows the following equations [34]:

$$W_x(z) = W_{0_x}\sqrt{1 + \left(\frac{z - z_{0_x}}{z_{R_x}}\right)^2} \equiv W_{0_x}\sqrt{1 + \left(\frac{M_x^2\lambda\,(z - z_{0_x})}{\pi W_{0_x}^2}\right)^2}, \tag{2.2.5}$$

$$W_y(z) = W_{0_y}\sqrt{1+\left(\frac{z-z_{0_y}}{z_{R_y}}\right)^2} \equiv W_{0_y}\sqrt{1+\left(\frac{M_y^2\lambda\left(z-z_{0_y}\right)}{\pi W_{0_y}^2}\right)^2}, \tag{2.2.6}$$

where W_{0_x} and W_{0_y} are the beam radii at beam waist in x- and y-direction, z_{0_x} and z_{0_y} are the locations of the beam waists, z_{R_x} and z_{R_y} are the Rayleigh ranges in x- and y-direction, and M_x^2 and M_y^2 are constants.

The propagation of a real beam thus depends, not only on the inverse of the beam radii at the beam waist, but also on constants M_x^2 and M_y^2. These constants are called beam quality factors or M^2 factors, and they describe how much the laser beam deviates from an ideal Gaussian beam in x- and y-direction [34]. Examining Equations (2.2.5) ja (2.2.6) at high z values, leads to an expression for the divergence half-angle far away from the focus for an arbitrary beam:

$$\theta = M^2\frac{\lambda}{\pi W_0}, \tag{2.2.7}$$

which means that the beam quality factor is defined as the beam parameter product, which is the product of beam radius at the beam waist W_0 and divergence half-angle θ, divided by λ/π [23]. By looking at Equation (2.1.14), it can be seen that λ/π corresponds to the beam parameter product of an ideal Gaussian beam. Thus, the beam quality factor of an ideal Gaussian beam is $M^2 = 1$, and for an arbitrary beam $M^2 \geq 1$. For this reason, it is often said that a laser beam is M^2 times diffraction-limited. Reasons for M^2 higher than 1 include the presence of higher propagation modes, and amplitude and phase distortions, for example due to inhomogeneity of the gain medium.

Because the Rayleigh range is defined as [34]

$$z_R = \frac{\pi W_0^2}{M^2\lambda}, \tag{2.2.8}$$

the divergence angle increases and the Rayleigh range becomes narrower when the beam quality factor M^2 increases or the beam radius at the beam waist w_0 decreases. Beam quality factor thus limits the focusability of a beam. Figure 2.3 shows the beam radius as a function of distance z for two beams that are focused to the same spot z_0, and have the same divergence angle, but their beam quality factors M_G^2 and M_{MM}^2 are different. The transversely multimode beam drawn in red color has a larger beam radius at the beam waist $W_{0_{MM}}$, and larger Rayleigh range $z_{R_{MM}}$ compared to

W_{0_G} and z_{R_G} of the ideal Gaussian beam drawn in blue color. This is because the transversely multimode beam has a beam quality factor larger than unity.

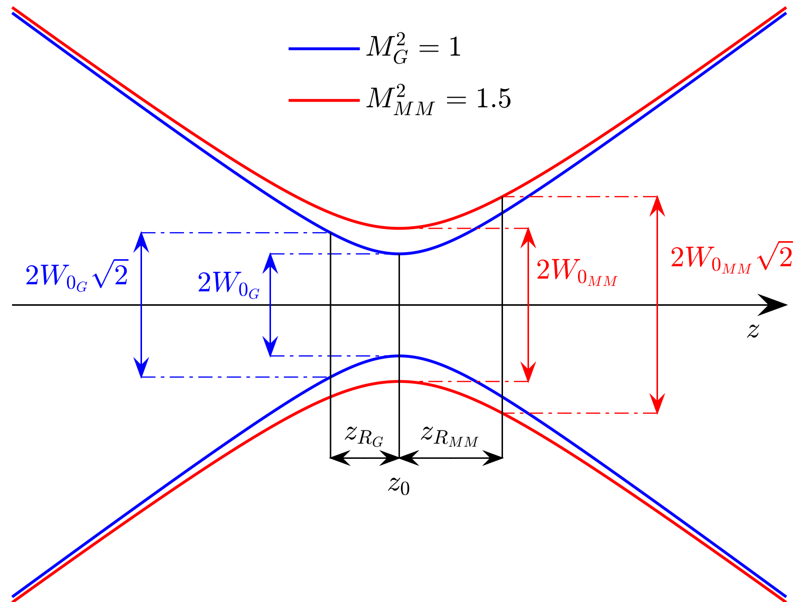

Figure 2.3 *Beam diameter shown as a function of distance for an ideal Gaussian beam (blue), and a transversely multimode beam (red), who both have the same divergence angle far away from the focus, but different M^2 factors.*

Equations (2.2.5) and (2.2.6) are valid for any perpendicular x- and y-axes that are in the transverse plane of the beam. However, choosing the x- and y-axes such that they are along the principal axes of the beam, will lead to the widest separation between the beam parameters, including the beam quality factors M_x^2 and M_y^2. This can be thought to give the most meaningful description of the beam. The principal axes of the beam correspond to the axes for which the cross moment $\overline{xy}$, calculated over the intensity profile, is zero. In practice, this corresponds to the axes that have the largest and smallest beam radius. With this formalism, the beam can then be characterized by the asymmetry of the beam waists ($W_{0_x} \neq W_{0_y}$), astigmatism ($z_{0_x} \neq z_{0_y}$), and the asymmetry of the divergence angle ($M_x^2/W_{0_x} \neq M_y^2/W_{0_y}$). [34]

2.3 Laser brightness

Laser brightness is often calculated when characterizing high power lasers. The brightness of a laser beam B is most often defined as the ratio between the power P, and the product of the area at the focus A, and the far field solid angle Ω [31].

That is

$$B = \frac{P}{A\Omega}. \tag{2.3.1}$$

The unit of brightness is thus W sr^{-1} cm^{-2}. The far field solid angle of an elliptic beam is

$$\Omega = \pi\theta_x\theta_y, \tag{2.3.2}$$

and the area of an elliptic beam at the focus is

$$A = \pi W_{0_x} W_{0_y}. \tag{2.3.3}$$

Utilizing Equation (2.2.7), the solid angle of an arbitrary beam can be calculated as

$$\Omega = \pi M_x^2 M_y^2 \frac{\lambda^2}{\pi^2 W_{0_x} W_{0_y}} = M_x^2 M_y^2 \frac{\lambda^2}{A}. \tag{2.3.4}$$

When this is substituted into Equation (2.3.1), the brightness of an arbitrary laser beam is obtained as

$$B = \frac{P}{M_x^2 M_y^2 \lambda^2}. \tag{2.3.5}$$

The brightness of a laser is thus directly proportional to the power, and inversely proportional to the M^2 factors and wavelength. Brightness describes the laser beam as a whole, taking into account all these three factors. It also does not change when the beam propagates, or when the beam passes through an optical element, provided that the optical element is diffraction-limited.

To achieve high brightness, the power of the laser must be maximized, while maintaining a good beam quality. This is often difficult to achieve, because the beam quality tends to deteriorate at high emission powers, as higher order lasing modes get excited, and nonlinear effects start to take place.

High brightness lasers, or lasers with high output power and good beam quality are the desired sources of light in many applications.

- High-brightness lasers are advantageous in various medical treatments, such as in eye surgery, which often require high power and small spot size. [18]
- In optical telecommunication, the efficient coupling of a laser to a single-mode fiber requires a good beam quality [21], and long-distance communication benefits from high power [12, p. 18].

- Material processing, micro-machining, and manufacturing require high-power lasers, which also have good beam quality to be able to focus the laser to a small spot with sufficiently large working distance. [29]

- Pump sources in solid-state lasers, fiber amplifiers, fiber lasers, and nonlinear frequency conversion require high power to be able to saturate the laser transition and maximize output power [28]. In addition, beams with high beam quality have wider Rayleigh range, which makes the alignment of optical elements in an optical system easier. Coupling efficiency to single-mode fibers and crystals is also higher when the M^2 factor is close to one [21].

While laser brightness is a useful parameter in many applications, it cannot characterize the laser completely, since it is just one number. For example, in some applications, the M^2 factor may be irrelevant, and instead it is more important to know the actual shape of the beam. Furthermore, there exists various other definitions for the brightness in the literature, and this often results in confusion.

2.4 Determining the laser beam quality

2.4.1 Measuring the M^2 factor

A typical way to measure the M^2 factors for a laser beam is to measure the change of the beam radius with propagation, and then fit Equations (2.2.5) and (2.2.6) to the data points. Usually the beam is first collimated, then focused, and the change in beam radius is measured in the vicinity of the focal plane of the focusing lens. The beam can be profiled, for example using a CCD camera, a pyroelectric camera, a knife-edge beam profiler or a scanning slit beam profiler. So that the profiler and the focusing lens can remain stationary, the beam can be focused to the profiler with a corner mirror consisting of two mirrors. This way, the distance from the focusing lens to the profiler can be altered by moving the corner mirror. Figure 2.4 illustrates a typical M^2 measurement setup, where a neutral density (ND) filter is used to attenuate the beam, in order to prevent the profiler from saturating.

In order to obtain the correct M^2 values, it is essential that the beam hits the detector perpendicularly, and that the beam does not move at the detector during the measurement. The wavelength of the beam must also be known, since the Equations (2.2.5) and (2.2.6) depend on the wavelength. The numerical aperture (NA)

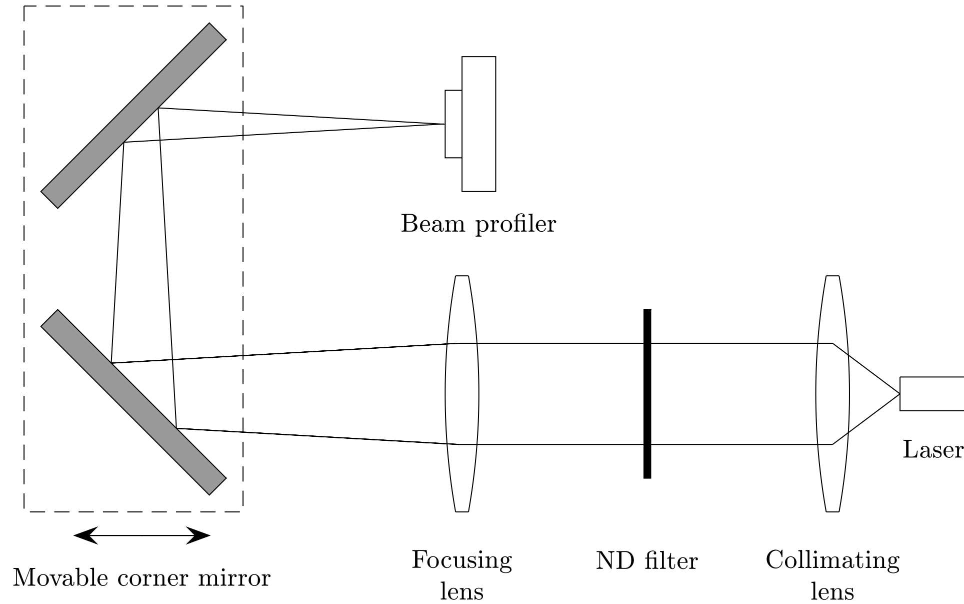

Figure 2.4 *A schematic figure of a typical M^2 measurement setup.*

of the collimating lens must be larger than the NA of the laser, in order to not clip the beam. The numerical aperture of a lens or laser in air is defined as

$$\mathrm{NA} = \sin\theta_0, \tag{2.4.1}$$

where θ_0 is the acceptance angle of the lens or the divergence angle of the laser.

According to ISO 11146 standard [10], the beam radius must be measured at least at 10 different distances. Around half of the points must be more than two Rayleigh lengths away from the focus, and the other half must be within one Rayleigh length from the focus. This is to achieve as good fit as possible to the measurement data.

Figure 2.5 shows an example of a beam quality factor measurement, where the beam radius has been measured as a function of distance. The blue crosses are the measurement points, and the uniform blue line is the fit that has been done using nonlinear regression with Equation (2.2.5). The boundaries of the Rayleigh range are labeled with a dashed line, and the points that are two Rayleigh lengths away from the focus are labeled with dash-dotted line. The resulting location of the beam waist z_0, beam radius at the beam waist W_0, and beam quality factor M^2 are listed in the bottom left corner of the figure.

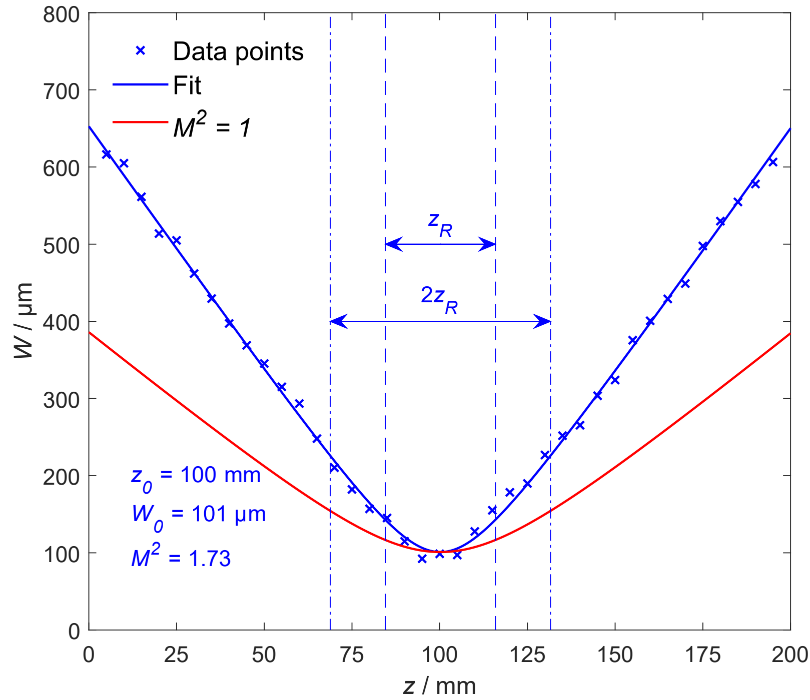

Figure 2.5 *An example of a beam quality measurement, where the beam radius W has been measured at different distances z, and the data is fitted using Equation* (2.2.5).

2.4.2 The effect of spherical aberrations on the M^2 factor

Especially when collimating the beam, but also when focusing the beam, one has to use diffraction-limited lenses, in order to minimize spherical aberrations. The spherical aberrations in spherical lenses degrade the beam quality, due to the fact that rays that are far away from the optical axis focus at different distance compared to rays that are close to the optical axis.

It can be shown that the beam quality that has been degraded by spherical aberrations can be written as [33]

$$M^2 = \sqrt{\left(M_0^2\right)^2 + \left(M_q^2\right)^2}, \tag{2.4.2}$$

where M_0^2 is the beam quality factor before the beam has passed through the lens, and M_q^2 is a parameter that depends on the spherical aberrations. For a spherical

lens, M_q^2 is defined as [33]

$$M_q^2 = \frac{2^{3/2}\pi C_4 W^4}{\lambda} \equiv \left(\frac{W}{W_q}\right)^4, \tag{2.4.3}$$

where W is the beam radius of the beam when it hits the lens, and

$$W_q = \left(\frac{\lambda}{2^{3/2}\pi C_4}\right)^{1/4} \tag{2.4.4}$$

is the critical beam radius, which corresponds to the beam radius, for which the beam quality factor of an ideal Gaussian beam degrades from $M_0^2 = 1$ to $M^2 = 1.414$. The critical beam radius can be thought as a limit, below which the spherical aberrations are relatively small. For beam radii larger than W_q the spherical aberration effects increase rapidly. C_4 is the quartic-aberration coefficient, which for a thin lens is defined as [19, p. 20–24]

$$C_4 = \frac{n^3 + (3n+2)(n-1)^2 p^2 + (n+2) q^2 + 4\left(n^2 - 1\right) pq}{32n(n-1)^2 f^3}, \tag{2.4.5}$$

where p and q are dimensionless parameters, n is the refractive index of the lens, and f is the focal length of the lens. Parameter q describes the shape of the lens, and for a thin lens it is defined as [33]

$$q = \frac{R_{s_2} + R_{s_1}}{R_{s_2} - R_{s_1}}, \tag{2.4.6}$$

where R_{s_2} and R_{s_2} are the radii of curvature of the first and second surfaces of the thin lens. Parameter p describes the input and output radii of curvature R_{in}, R_{out} of the wave with respect to the focal length of the lens, so that [33]

$$R_{\text{in}} = \frac{2f}{p+1}, \;\; R_{\text{out}} = \frac{2f}{p-1}. \tag{2.4.7}$$

Figure 2.6 shows M^2 as a function of the beam radius W for an ideal Gaussian beam $\left(M_0^2 = 1\right)$, which is focused or collimated with a plano-convex lens with a focal length of f. In the case of beam focusing, the input beam is collimated, meaning that $R_{\text{in}} = \infty$. By using Equation (2.4.7), it can then be calculated that $p = -1$. In the case of beam collimation, the output beam is collimated, meaning that $R_{\text{out}} = \infty$,

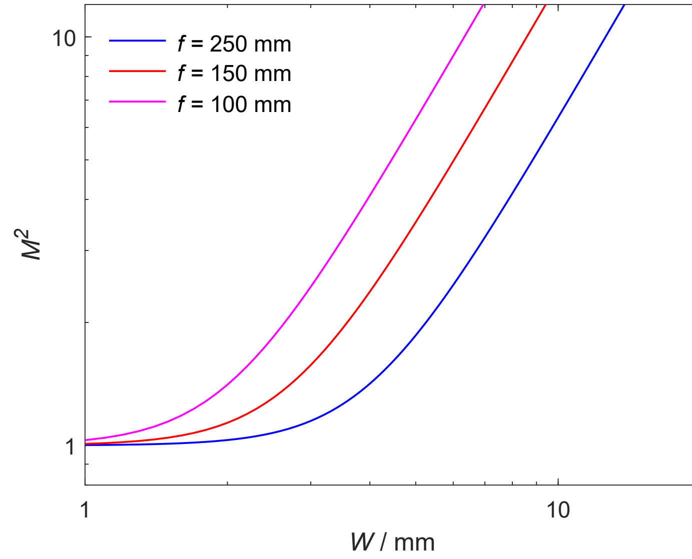

Figure 2.6 *The simulated beam quality factor M^2 given as a function of the beam radius W for an ideal Gaussian beam $(M_0^2 = 1)$, when the beam is focused or collimated with a plano-convex lens with a focal length of f. In collimation, the beam enters the planar side of the lens, and, in focusing, the beam enters the convex side of the lens.*

and thus $p = 1$. When focusing the beam, the spherical aberration effects are the smallest when the beam enters the lens from the convex side $(R_{s_2} = \infty)$ [33], and, by using Equation (2.4.6), it can be calculated that $q = 1$. On the other hand, when collimating the beam, the beam should enter the lens from the planar side $(R_{s_1} = \infty)$ to minimize the spherical aberration effects [33], so that $q = -1$.

It can be seen from Figure 2.6, that the smaller the focal length of the lens is, the stronger the spherical aberration effects. The critical beam radius for the lens with $f = 100$ mm is $W_q \approx 2$ mm, whereas for the lens with $f = 250$ mm it is $W_q \approx 4$ mm. Thus, if a spherical lens is used to focus the beam in a beam quality measurement, a lens with as large f as possible should be used, in order to minimize spherical aberration effects.

2.4.3 Beam profiling methods

In order to define the beam radius, a suitable measurement method is needed. The most commonly used beam profilers in beam quality measurements are CCD (charge-coupled device) or CMOS (complementary metal oxide semiconductor) camera, pyroelectric camera, scanning slit beam profiler, and knife-edge beam profiler, which

are all based on converting the input light signal into an electrical signal. The basic working principle of each of these devices, as well as the sources of noise and noise treatment are described here.

CCD camera and CMOS camera

CCD and CMOS cameras consist of a matrix of pixels, where each pixel has a potential well, which confines the charge carriers. The incoming photons are absorbed by the pixels, forming electron-hole pairs, which leads to an electric signal that can be measured separately for each pixel. The number of electrons that are collected is directly proportional to the intensity level and the exposure time. [24]

Figure 2.7 shows a schematic of the structure of a pixel in a CCD camera, which typically consists of three electrodes. By applying a positive voltage to one of the electrodes, the electrostatic potential of the underlying silicon structure can be changed, and a potential well is formed beneath the electrode. The neighboring gates are biased negatively to form potential barriers to help confine the electrons. By modulating the voltages applied to the electrodes, the charge carriers can be transferred to the output amplifier, and converted to a voltage signal. [15]

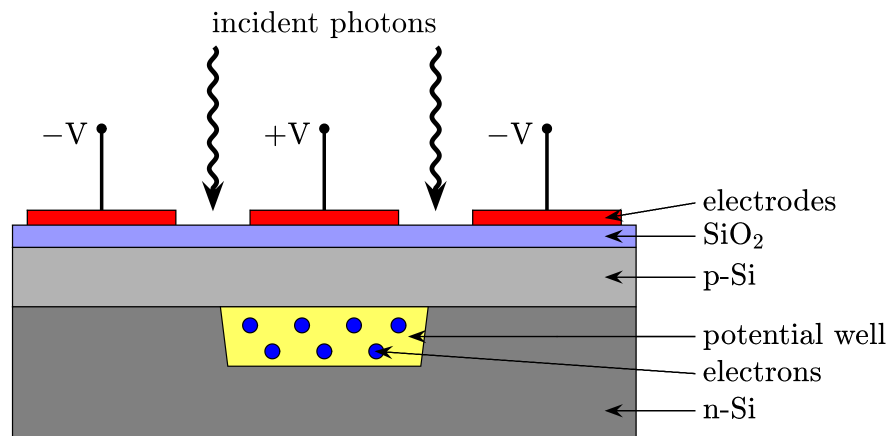

Figure 2.7 *Schematic figure of the structure of a pixel in a CCD camera.*

While in CCD cameras, the photogenerated charge needs to be transferred across the chip to the output amplfier, in CMOS cameras, each pixel has its own charge-to-voltage conversion, which also often includes amplifiers, noise-correction, and digitization circuits. This increases the complexity of the device, and reduces the area

available for capturing light. Since each pixel converts the charge to voltage separately, the uniformity is typically poorer compared to CCD cameras. The dynamic range is also narrower than in CCD cameras. [1]

The resolution of a CCD or CMOS camera depends on the size of a single pixel, which depends on the sensor type. The accurate measurement of beam radius requires at least around 5 pixels [24], which limits the smallest beam size that can be measured. The size of the sensor can be many millimeters, which means that relatively large beams can be measured.

The quantum efficiency is the average probability that a photon generates an electron-hole pair. The quantum efficiency depends on the material of the sensor, and the wavelength of the photon [4], which also means that different wavelengths require a different type of sensor. Table 2.1 shows the most common sensor types, the measurable wavelength range, a typical pixel size, and the the smallest beam radius that can be measured.

Table 2.1 *The most common CCD sensor types, the corresponding measurable wavelength range, a typical pixel size, and the smallest beam radius that can be measured. [3]*

Sensor type	**Wavelength / nm**	**Typical pixel size / µm**	**Min. beam radius / µm**
Si	400–1100	5	25
Phosphor-coated Si	1440–1605	50	250
InGaAs	900–1700	10–30	50–150

CCD cameras are typically very sensitive to light, meaning that the laser beam must be attenuated before it hits the camera. CCD cameras also have a very low dynamic range, which is the ratio between the largest and the smallest signal that can be measured with a specific exposure time. This is partly due to the small size of the pixels, which leads to a low electron capacity for the quantum wells. A CCD camera with a larger pixel size has a higher dynamic range and signal-to-noise ratio (SNR), but a lower resolution. Because CCD cameras measure the intensity for each pixel separately, they will measure the actual 2D intensity profile of the laser beam. [36]

Pyroelectric camera

A pyroelectric camera consists of an array of pyroelectric crystal elements, which utilize a pyroelectric material, such as $LiTaO_3$. Photons that are incident on the crystal are absorbed and converted to heat, which polarizes the pyroelectric crystal. This generates a charge on the surface, whose magnitude is proportional to the absorbed heat. [8]

Figure 2.8 shows a circuit of a simple pyroelectric crystal element. It consists of a thin pyroelectric crystal, which is metallized on both sides to collect the charge that is generated. Parallel to the crystal is a capacitor that produces a voltage, which is proportional to the energy, and a resistor that bleeds off the generated charge, so that the detector is ready for the next measurement. [8]

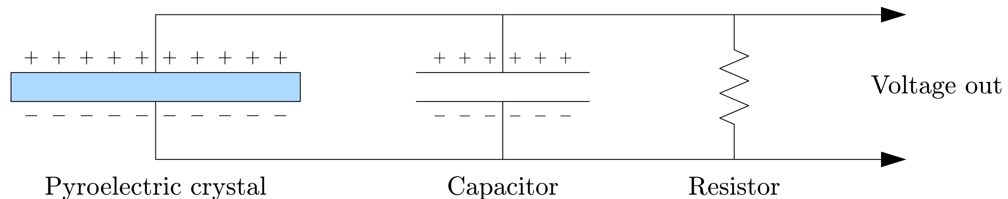

Figure 2.8 *Schematic figure of the circuit of a pyroelectric element.*

The pyroelectric crystal can only measure change in intensity, which means that a continuous signal needs to be chopped in order to create a changing signal. A typical pyroelectric camera includes an integrated chopper for this purpose. [8]

Pyroelectric cameras have an extremely wide spectral range, and they can be used to profile beams from the ultraviolet (UV) region to the far infrared (FIR) region [3], something that is difficult to achieve with a CCD camera. However, pyroelectric cameras have a much larger pixel size than CCD cameras, which greatly limits their resolution. For example, a typical effective pixel size for a $LiTaO_3$ camera is around 80 µm [3], which means that the smallest measurable beam radius is 400 µm, and thus only relatively large beams can be measured.

Scanning slit beam profiler and knife-edge beam profiler

Scanning slit and knife-edge beam profilers utilize the moving-slit method, where there is an aperture between the laser beam and the photodetector, that is scanned over the laser beam. The strength of the measured signal is directly proportional to the intensity passing through the aperture. There are three main types of apertures that are used: pinhole, slit, and knife-edge. All of these aperture types are illustrated in Figure 2.9. The intensity profile that is obtained is different for each aperture type. The slit and the knife-edge scan the whole beam with one sweep, while the pinhole scans only a particular part of the beam at once, and requires a raster scan of the beam. [11, p. 28–29]

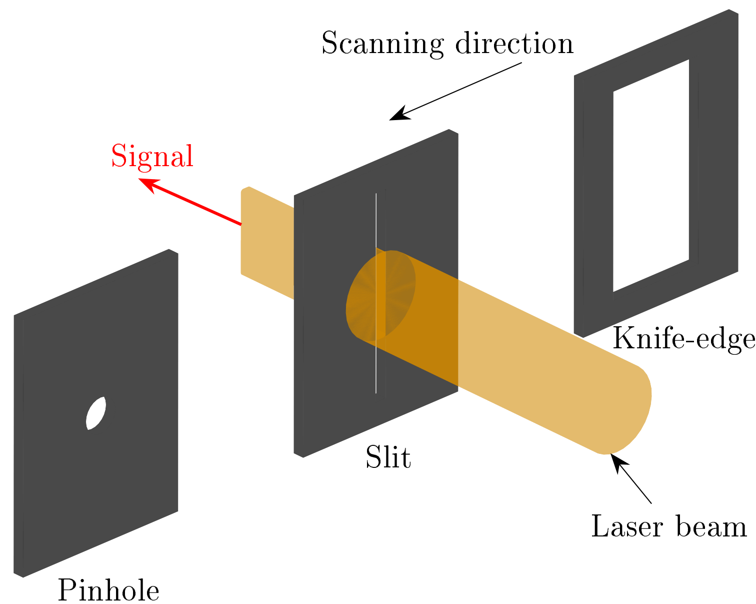

Figure 2.9 *The aperture types of the scanning slit and knife-edge beam profiler.*

Figure 2.10 shows a typical structure of a scanning slit or knife-edge beam profiler. The profiler consists of a rotating drum that is tilted at 45°. The drum has two slits with the same width, which scan the beam at two orthogonal directions. Because the slits rotate around a circular path, the measurement is not planar, but since the circumference of the drum is much larger than the beam size, the errors that are caused by this are negligible. The scanning orientation is usually adjustable, meaning that any elliptic beam that propagates in an arbitrary angle can be measured. [11, p. 29–31]

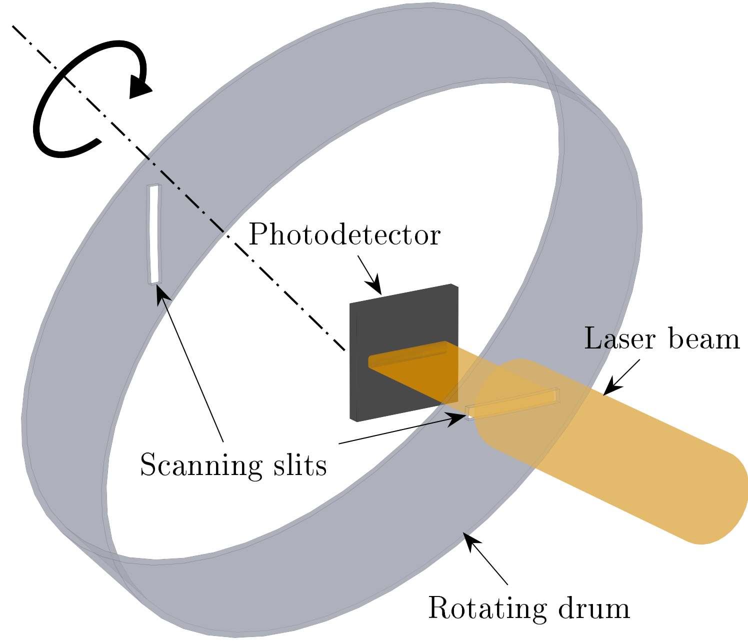

Figure 2.10 *The structure of a typical scanning slit or knife-edge beam profiler.*

Because of the large size of the detector, and because only a small part of the beam hits the photodetector at once, the dynamic range of an scanning slit beam or a knife-edge profiler is high. By using a suitable photodetector, all wavelengths from UV range to FIR range (190 nm–over 100 μm) can be measured [7]. Contrary to a CCD camera or pyroelectric camera, scanning slit or knife-edge beam profiler only measures the integrated intensity distributions in two orthogonal directions, and as such it is unable to obtain direct information about the actual 2D intensity distribution.

The finite width of the slit has an effect on the shape and width of the obtained intensity distribution. If it is assumed that the actual profile is of the Gaussian form:

$$G(z) = e^{-r^2}, \tag{2.4.8}$$

the measured profile can be expressed as

$$M(z) = \frac{\operatorname{erf}(r + aX) - \operatorname{erf}(r - aX)}{2 \times \operatorname{erf}(aX)}, \tag{2.4.9}$$

where

$$\operatorname{erf}(x) = \frac{1}{\sqrt{\pi}} \int_{-x}^{x} e^{-t^2} dt \tag{2.4.10}$$

is the error function,

$$X = \frac{s}{W} \tag{2.4.11}$$

is the ratio of the width of the slit s and the beam radius W, and

$$a = \sqrt{-\ln(b)}, \tag{2.4.12}$$

where b corresponds to the fraction of the peak intensity at the center, at the points between which the beam width is measured. [11, p. 59–62]

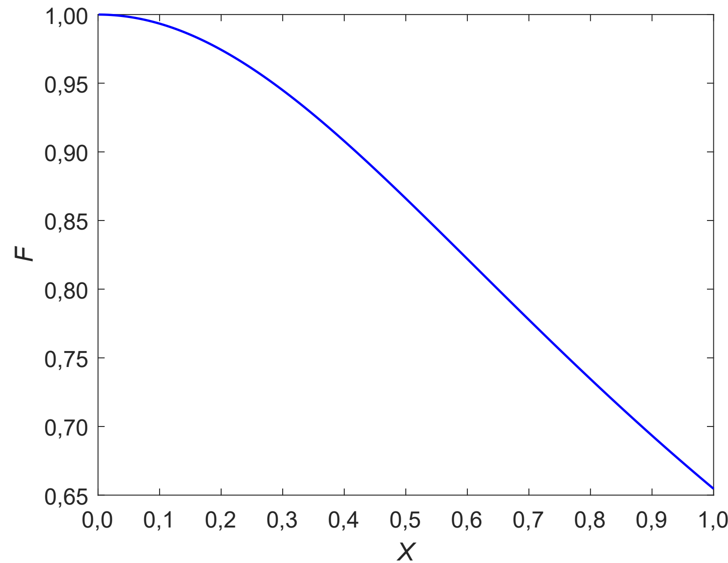

Figure 2.11 *The ratio of the true width and the measured width F given as a function of the ratio of the width of the slit and the beam radius X.*

Figure 2.11 shows F, which is the ratio of the true width and the measured width, as a function of X. For a Gaussian beam, the beam radius obtained by the D4σ method is the same as the $1/e^2$ width, which corresponds to $b = 0.1353$. As is evident from the figure, when X increases, i.e. when the width of the slit increases or the beam radius decreases, the error in the measured beam radius increases. When the width of the slit is 40% of the beam radius, the measured beam radius is around 10% larger than the actual beam radius.

Figure 2.11 can be used to correct the measured beam radii only when the beam radius is defined as the $1/e^2$ width, and as such it does not apply to non-Gaussian beams, whose $D4\sigma$ width differs from $1/e^2$. For non-Gaussian beams, the width of the slit should be at least an order of magnitude smaller than the beam radius, in

order to prevent any significant errors introduced by the finite width of the slit.

Noise in beam profilers

Noise is unavoidable, regardless of the beam profiling method. The amount of noise limits the smallest measurable signal, and will have a detrimental effect on the calculated beam radius if it is not treated properly. Usually the noise forms a Gaussian distribution with a certain variance, which can be used to describe the magnitude of the noise. Each profiling method has its own sources of noise, and these are briefly described here.

The main sources of noise in a pyroelectric camera are:

- **Temperature noise:** This noise is caused by the thermal excitation of charges. It is the smallest source of noise, and it is also dependent on the temperature, meaning that it can be decreased by cooling down the camera. [6]
- **Dielectric noise:** Because dielectric materials are not perfect capacitors, the pyroelectric element has dielectric resistance, which causes dielectric noise, also known as Johnson noise. [6]
- **Amplifier noise:** This is caused by the electric amplifier of the detector. The magnitude of the noise is dependent on the type of amplifier that is used. [6]

The main sources of noise in a CCD or CMOS camera, and scanning slit profiler are:

- **Dark noise:** Even when photons do not hit the camera, there exists dark current, caused by the spontaneous excitation of charge carriers. Dark current leads to dark noise. It is proportional to the temperature, which means that it can be decreased by cooling down the camera. [5]
- **Read noise:** When the current signal is transformed into an electronic signal, it causes read noise, which is not dependent on the signal level or the temperature. [5]

- **Photon shot noise:** This is purely statistical noise, and is caused by the randomness of photons. It is proportional to the signal level, and does not depend on the temperature. [5]
- **Fixed pattern noise:** This is a noise that is only present in CCD cameras, and it is due to the spatial non-uniformity of the pixels. It can be neglected in high quality scientific CCD cameras. [5]

The peak of the noise distribution is usually not located at zero by default, i.e. the noise oscillates around a non-zero value. This is called the noise baseline, and it is mainly caused by ambient light. This problem can be solved by calculating the noise baseline for each pixel, and subtracting it to obtain a zero baseline. For scanning slit beam profilers, which utilize a single photodetector, the baseline can be calculated on the fly from areas on the detector that do not receive any signal. In contrast, for pyroelectric and CCD cameras, the laser must be blocked or turned off, and the baseline should then be calculated at different exposure times. The resulting baselines are then subtracted for each pixel. The problem is that the baseline may drift due to changes in ambient light levels or the temperature of the camera, and this will lead to incorrect measurement results. To avoid baseline drift and errors in the measurements, the temperature of the camera should be allowed to stabilize before doing any measurements, ambient light hitting the beam profiler should be minimized, and the baseline calculation should be performed regularly and at the start of each measurement.

In order to define the beam radius accurately, the signal-to-noise ratio (SNR) must be large enough. This is especially important when the $D4\sigma$ method is used in calculations, due to the fact that the beam wings have a big influence on the obtained beam radius. Thus, if the SNR is not large enough, the beam radius will be overestimated. To achieve a good SNR, the signal strength should be maintained as high as possible during the measurements, which may be difficult if the dynamic range of the beam profiler is narrow, such as in CCD and CMOS cameras. The magnitude of the noise may also be decreased by averaging over multiple frames, which allows weaker signals to be measured. However, this requires that the beam does not move and remains stable during the averaging.

ISO-11146-3 standard [9] recommends that a virtual aperture is defined around the beam. The aperture should be centered at the beam centroid, and it should be three times the $D4\sigma$ diameter in size. Measurement points outside the aperture should

be neglected. However, it can be shown [2] that an aperture, which is two times the $D4\sigma$ diameter in size works better, as it leads to smaller error in measurements. When working with a 2D intensity distribution, such as with a CCD, CMOS or pyroelectric camera, an elliptically shaped aperture seems to work the best.

3. EDGE-EMITTING SEMICONDUCTOR LASERS

In this chapter, the basic theory of edge-emitting lasers (EELs) is explained, and the structure and design principle of the two EEL types, RWG lasers and tapered lasers, that are analyzed in this thesis are introduced.

3.1 Basic structure of edge-emitting lasers

Laser diodes are semiconductor devices that are pumped electrically to achieve population inversion. A simple laser diode consists of two doped semiconductor layers, an n-doped and a p-doped semiconductor, which form a p-n junction. When an electric current flows through the structure, electrons and holes recombine at the junction, emitting photons. In EELs, the laser cavity is located in the plane of the laser chip, where the cleaved facets act as mirrors. When the gain overcomes the losses, lasing begins, and relatively coherent light is emitted. [14, p. 1–2]

Laser diodes are often mounted on a submount, which acts as a heat spreader, and which is made of a material whose coefficient of thermal expansion (CTE) matches that of the laser diode. Figure 3.1 shows a schematic picture of an EEL chip mounted on a submount. The device is operated by applying a forward bias between the cathode and the anode, which is wired to the p-side electrode of the EEL chip.

A typical EEL utilizes a p-i-n structure, where a waveguide (WG) made of an intrinsic semiconductor is sandwiched between p- and n-doped semiconductor layers. The band gap of the intrinsic layer is usually smaller than the band gap of the surrounding p- and n-layers, and thus it will confine the charge carriers, while also acting as a WG for the optical field. This type of structure leads to a low threshold current, and a high recombination efficiency. [14, p. 10–11]

To further increase the recombination efficiency, quantum wells (QW) can be imple-

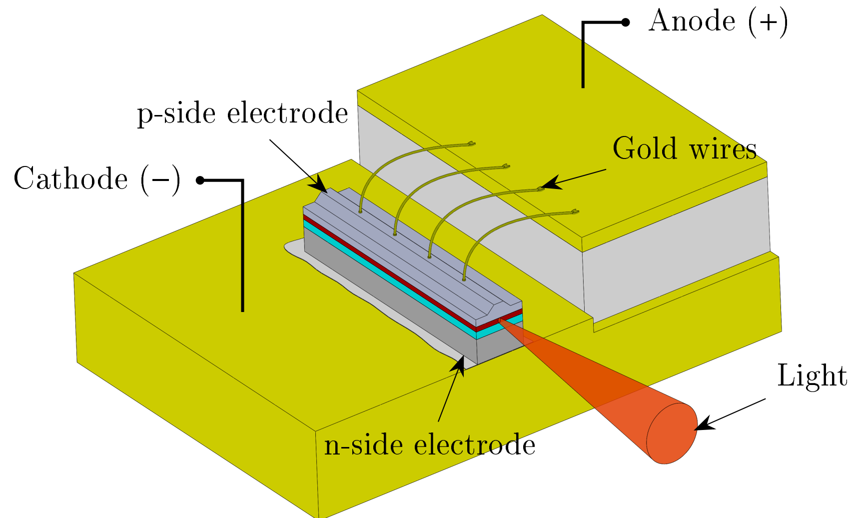

Figure 3.1 *Schematic picture of an edge-emitting laser mounted on a submount.*

mented into the structure. QW structures are made of thin, around 10 nm thick semiconductor layers that are sandwiched between barrier layers that have a higher band gap. This confines the charge carriers into a thin active layer, which causes the wave functions of the electrons and holes to be quantized. The emission wavelength depends on the composition of the barrier layers and the QW, as well as on the thickness of the QW. [14, p. 12, 509–516]

3.2 Ridge waveguide lasers

Besides confinement in the vertical direction, the current, charge carriers or photons must be confined in the lateral direction. In this section, an EEL called RWG laser is introduced. The structure and output beam divergence of RWG lasers are explained in the following subsections. The implementation of a DBR into the structure to achieve single-frequency operation is also briefly explained.

3.2.1 Structure of ridge waveguide lasers

RWG lasers are index-guided lasers that combine current confinement with weak photon confinement. In RWG lasers, material is etched down close to the active area

to form a ridge, and the current is injected from the top of the ridge into the laser chip. A schematic figure of an RWG structure is shown in Figure 3.2. The width of the ridge w_{RWG}, and the etch depth t_{RWG} can be adjusted in such way that there is large enough effective lateral index change to achieve single-mode optical field in the lateral direction. [14, p. 29]

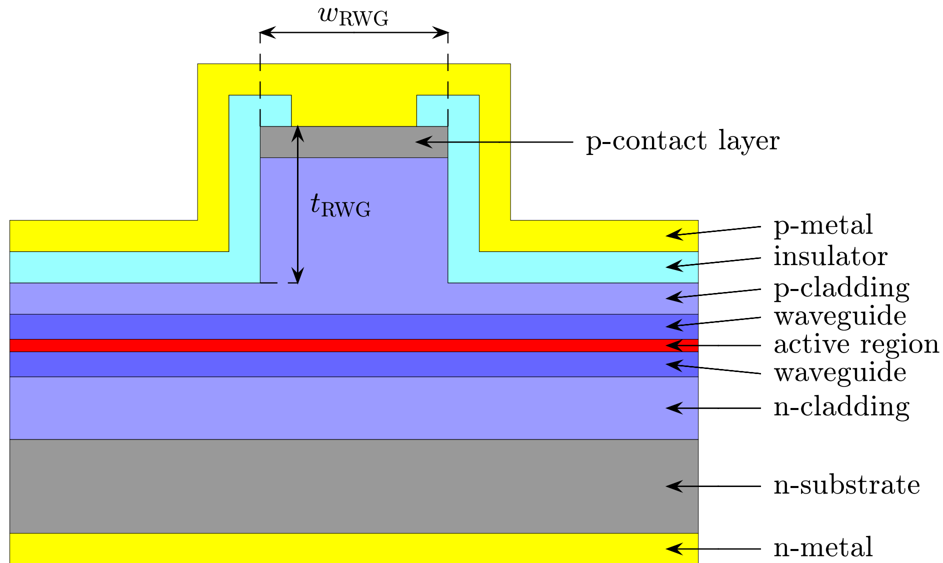

Figure 3.2 *Schematic picture of the cross section of a ridge waveguide laser (not to scale). Lateral confinement of the optical field is achieved by the ridge structure, and current confinement is achieved by driving current through a thin contact formed by an insulating layer at the top of the ridge.*

The width of the optical field in the lateral direction is narrow in RWG lasers, which leads to high intensity. Too high intensity leads to COD, where the junction absorbs too much energy due to non-radiative recombination, which causes the laser facet to melt and recrystallize [14, p. 32]. This limits the output of RWG lasers to relatively low power [30].

3.2.2 Output beam divergence

Due to the fact that the size of the output aperture is different in the lateral and vertical direction, the divergence angle is also different, which means that the output beam is elliptical. In order to achieve close to single-mode operation in the vertical direction, the output aperture is typically in the order of 1 μm [25]. Looking at Equation (2.2.7), this leads to a broad divergence angle. Due to the fact that the

beam divergence is fast in the vertical direction, it is commonly called the fast axis (FA) [25].

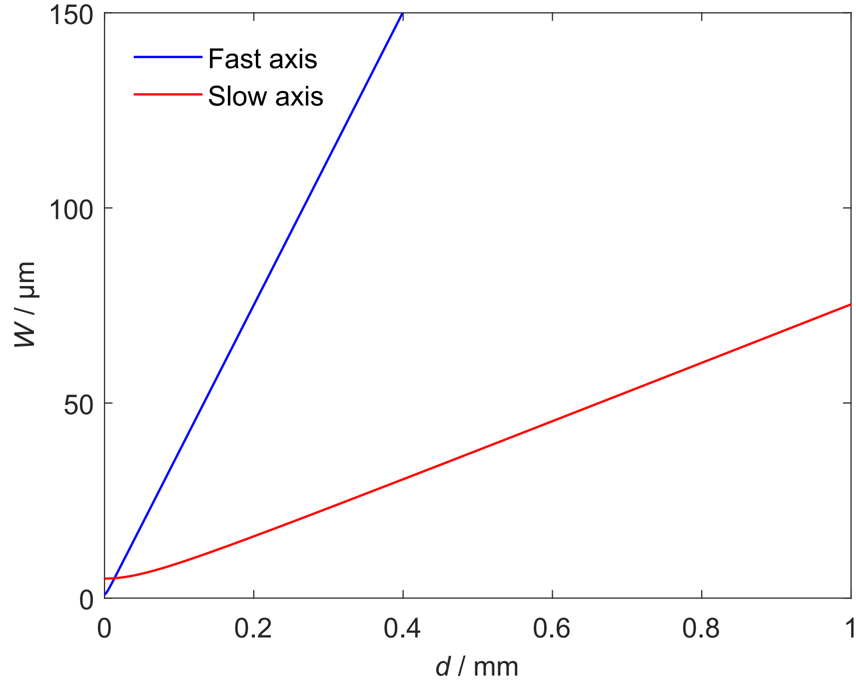

Figure 3.3 *The beam radius W as a function of distance from the facet d for the fast axis (blue) and slow axis (red) of a ridge waveguide laser. Smaller output aperture leads to a broader divergence in the fast axis direction.*

The output aperture in the lateral direction is wider, but the beam quality is still close to $M^2 = 1$, provided that the ridge width and the etch depth are optimized. This leads to a smaller divergence half-angle than in the FA direction. Due to the fact that the divergence is slower in the lateral direction, it is commonly called the slow axis (SA) [25]. A schematic of typical FA and SA divergence behavior of an RWG laser is shown in Figure 3.3.

The FA divergence is typically larger than 30°, which means that a lens with a high NA value is required to collimate the beam. The high divergence angle means that the Rayleigh range is very narrow, which makes the alignment of the collimation lens difficult.

The high FA divergence can be mitigated by utilizing a wider WG in the epitaxial structure. Typically this leads to weaker optical confinement, and allows higher order modes to propagate. The propagation of higher order modes can be avoided with

an asymmetrical structure, where the thickness of the WG above the QWs differs from the thickness of the WG below the QWs. This kind of asymmetrical WG also decreases the series resistance of the structure. Since the beam radius is larger, the intensity at the facet is reduced, and COD is pushed back to higher output powers, implying that higher output powers are achievable. [37]

3.2.3 Distributed Bragg reflector

A DBR is a periodic structure that consists of alternating layers of two different optical materials. The ray components reflecting from the interfaces interfere constructively for a certain wavelength, leading to strong reflection at this wavelength. By designing the DBR in such way that the gain maximum coincides with the maximum reflection, the laser will operate at a single longitudinal mode with a narrow bandwidth [20, p. 75–76].

The grating period Λ, which leads to constructive interference at wavelength λ is given by the Bragg condition [20, p. 70–76]:

$$\Lambda = q\frac{\lambda}{2n_{\mathrm{eff}}}, \tag{3.2.1}$$

where q is the order of reflection, and n_{eff} is the effective refractive index of the DBR. The reflectivity is determined by the number of layers, as well as the refractive index contrast between the optical materials that are used. The reflection bandwidth in spectral domain is mainly determined by the refractive index contrast. [14, p. 92]

One way to implement a DBR to an RWG laser is to implement it as an etched through surface grating to one end of the cavity by utilizing lithographic methods. The grating is etched into the the cladding to avoid any detrimental effects on the structure caused by etching the waveguide. In order for there to be good coupling of the surface grating with the optical field, there must be sufficient penetration of optical field tails in the cladding. By implementing a DBR to a RWG laser cavity, single-frequency operation with a narrow bandwidth can be achieved [14, p. 92]. Figure 3.4 illustrates an RWG laser with a DBR implemented to one end of the cavity.

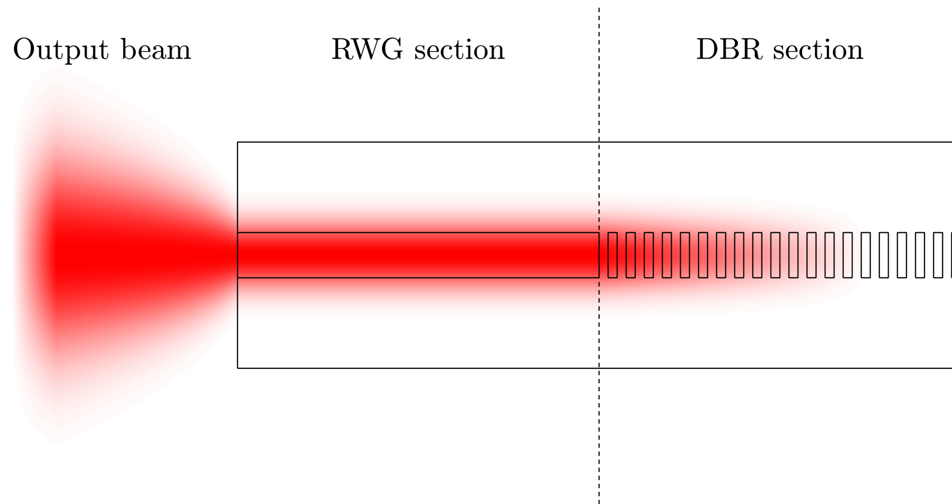

Figure 3.4 *A schematic of a DBR laser. A DBR is implemented into one end of the cavity of an RWG laser to achieve single-frequency operation.*

3.3 Tapered power amplifier lasers

In this section another EEL called tapered power amplifier laser is introduced. Its basic structure, nonlinear effects, and design parameters are explained in the following subsections.

3.3.1 Structure of tapered lasers

A tapered power amplifier laser is a high-brightness broad-area laser. It consists of a lateral single-mode laser, and a tapered gain medium, which can be either gain-guided or index-guided. Both of these are integrated into the same chip, so that the whole chip acts as an unstable resonator. When the single-mode beam is shot into the tapered power amplifier, it gets broadened and amplified. Thus, the intensity at the output facet is decreased, which prevents COD from occurring, and makes it possible to achieve several watts of output power. The basic structure of a tapered laser is illustrated in Figure 3.5. The beam quality of tapered lasers is much better compared to gain-guided broad-area lasers, because the beam radius at the beam waist is smaller, while the divergence angle is the same magnitude. [37]

The curved wavefronts of the tapered laser get diffracted at the output facet according to Snell's law. In the vertical direction the beam diverges from the output facet, while in the lateral direction the beam diverges from a virtual point source, which is

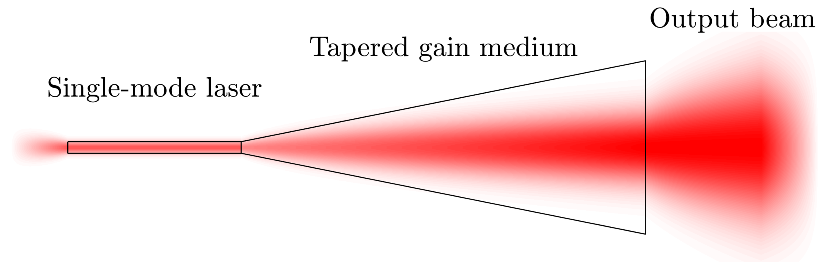

Figure 3.5 *A schematic of a tapered laser. The transversely single-mode beam produced by the RWG section is broadened and amplified in the tapered section.*

approximately $L_{\text{taper}}/n_{\text{eff}}$ behind the output facet, where L_{taper} is the length of the tapered section, and n_{eff} is the effective refractive index of the epitaxial structure. Thus, the length of the tapered section has a significant effect on the astigmatism of the output beam. Because the output beam is astigmatic, collimation of the beam requires two lenses, with at least one of them being a cylindrical lens.

3.3.2 Nonlinear effects in tapered lasers

Nonlinear effects, such as self-focusing and filamentation, are relevant in tapered lasers, and they will limit the output power and brightness. Self-focusing is a nonlinear effect where the beam gets focused due to change in the refractive index of the material at the propagation axis. In tapered lasers, the refractive index change is caused by spatial hole burning (SHB) and thermal lensing. In filamentation, the beam is broken into several smaller beams with smaller powers. Filamentation is caused by the same effects, but typically it occurs at optical powers far above the self-focusing limit. Self-focusing and filamentation narrow the far field divergence, broaden the beam radius, cause changing astigmatism, and degrade the beam quality. [13]

When the output power of a tapered laser is increased, the photon density at the propagation axis is increased, which causes the charge carrier density to decrease due to stronger stimulated recombination. This is called SHB. Thus, the profile of the charge carrier density gradually changes into a 'rabbit-ear' shape with maxima at the edges, and a minimum at the center. Because of this, the refractive index at the propagation axis is higher, which causes a WG to form at the propagation axis. This concentrates the intensity to the center of the beam, which in turn strengthens SHB, and the WG effect. Eventually, the strong feedback will cause self-focusing and filamentation. [13]

The local absorption of free charge carriers in the high photon density region at the propagation axis will raise the temperature, and thus the refractive index. This effect is known as thermal lensing, because it causes a parasitic thermal WG to form, which eventually leads to self-focusing and filamentation. On the other hand, this effect is compensated by the heat generated by non-radiative recombination of charge carriers at the edges of the beam, where the charge carrier density is the highest. [13]

3.3.3 Design of tapered lasers

The beam quality of the output beam is influenced by the length of the RWG L_{RWG} and tapered regions L_{taper}, the opening angle of the tapered region θ_{taper}, the input drive current I, as well as the coating of the facets [13]. The structure of a tapered laser with all the design parameters is shown in Figure 3.6. All of these parameters need to be optimized to achieve good beam quality, and thus high brightness.

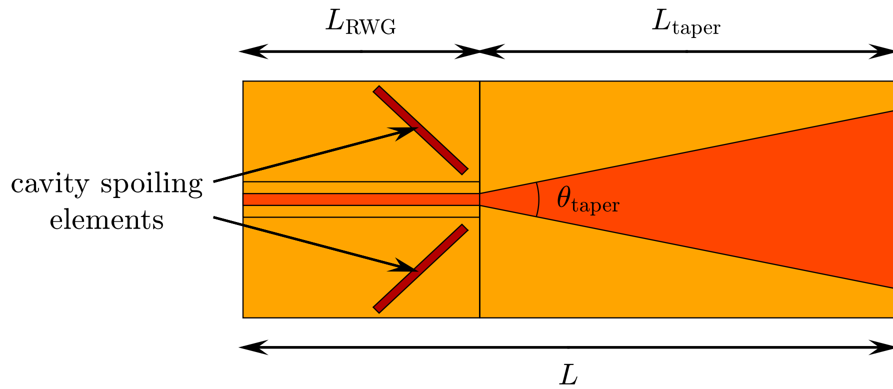

Figure 3.6 *A schematic presentation of the structure and design parameters of a tapered laser.*

The transversely single-mode laser region, which is often an RWG structure, should support only the fundamental mode, so that it dampens any higher order modes that are produced by the tapered region as the field is reflected back and forth between the facets. The filtering effect may be improved by either increasing the length of the RWG region or by implementing cavity spoiling elements outside the active region. Cavity spoiling elements are deep grooves that are etched through the structure, and thus they prevent the optical field from propagating outside the active region. Cavity spoiling elements suppress any side lobes that are present at

the output facet, thus decreasing the self-focusing effect. This will improve the beam quality. [13]

The opening angle of the tapered region should be close to or slightly smaller than the free diffraction angle in order to achieve a good overlap between the optical field and the gain- or index-guided tapered region. This decreases SHB and thus self-focusing. This leads to a better M^2 and higher brightness. [13]

Longer tapered sections lead to an increased maximum output power, as well as an increased lasing threshold current, due to the larger area of the laser. The beam quality of a longer laser chip is better, because it improves thermal dissipation, and decreases the photon density in the tapered section. This mitigates the SHB effect, and as a consequence it delays the self-focusing effect to higher output powers. Thus, the tapered section should be made as long as possible, within the practical limits. [13]

The output facet should have an anti-reflective (AR) coating to minimize the field that gets reflected back into the chip, in order to minimize the excitation of higher order modes. The reflectance at the back facet should be maximized, which can be achieved with a high-reflective (HR) coating, or an AR-coated DBR.

The output power and beam quality can be adjusted by driving current separately into the RWG region and the tapered region. This can be achieved by having a separate electrode for both of these regions. The RWG region should be driven with a small current to achieve single-mode emission, and the output power can be modulated by driving current into the tapered region.

4. SAMPLES AND CHARACTERIZATION METHODS

In this chapter, the structure of the laser components that were analyzed is introduced. The characterization methods that were used to analyze tha samples are also described.

4.1 Sample structures

The beam quality of two different EEL types was analyzed: RWG lasers and tapered lasers. The goal was to achieve transversely single-mode behavior, with maximized output power. This equals to maximizing the brightness.

All of the samples were grown using the molecular beam epitaxy (MBE) method. Two types of epitaxial structures were used: a symmetric and an asymmetric structure. These are shown in Figure 4.1. In the asymmetric structure the thickness and bandgap of the WG is different above and below the QWs. The WG is also thicker in the asymmetric structure compared to the WG in the symmetric structure. In addition, the number of QWs is different. The target emission wavelengths were 1180 nm and 1154 nm for the symmetric and asymmetric structures, respectively.

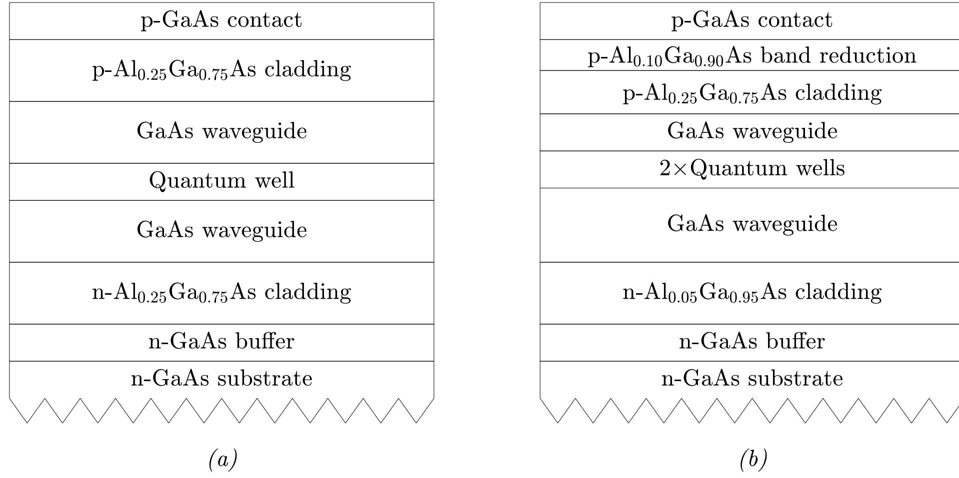

Figure 4.1 *(a) Symmetric, and (b) asymmetric epitaxial structures that were used in the samples.*

For the RWG lasers, both the symmetric and asymmetric structures were analyzed using different ridge widths w_{RWG} and etch depths t_{RWG}. This was to find out the parameters that lead to the highest brightness. The w_{RWG} and t_{RWG} values that were analyzed are listed in Tables 4.1 and 4.2. Other than the etch depth t_{RWG}, the exact same process was used for both RWG structures.

Table 4.1 *The nominal ridge widths w_{RWG}, and etch depths t_{RWG} that were analyzed for the symmetric structure.*

Etch depth $t_{\mathbf{RWG}}$ / nm	**Ridge width $w_{\mathbf{RWG}}$ / µm**
1120	2.0, 3.0, 3.5, 6.0
1270	2.5, 3.5, 5.5
1300	2.5, 3.5

Table 4.2 *The nominal ridge widths w_{RWG}, and etch depths t_{RWG} that were analyzed for the asymmetric structure.*

Etch depth $t_{\mathbf{RWG}}$ / nm	**Ridge width $w_{\mathbf{RWG}}$ / µm**
1280	4.0
1580	4.0, 5.0

Two tapered lasers were analyzed. Both components included an etched through DBR implemented to one end of the chip. The epitaxial structure of the lasers was

Table 4.3 *The nominal design parameters of the tapered laser components (see Figures 3.2 and 3.6 for definitions).*

Parameter	Value
θ_{taper}	5°
L_{taper}	4 mm
L_{RWG}	1 mm
L_{DBR}	2 mm
w_{RWG}	3.2 µm
w_{DBR}	3.2 µm
t_{RWG}	1350 nm
t_{DBR}	1400 nm

symmetrical (Figure 4.1(a)). The two lasers had nominal DBR periods of 519.0 nm and 519.9 nm, respectively, which leads to third-order Bragg reflection around the target emission wavelength of 1180 nm (see Equation 3.2.1). Other parameters were the same, and they are listed in Table 4.3. The parameters L_{DBR}, w_{DBR}, and t_{DBR} are the length, width, and etch depth of the DBR, respectively. The widths and etch depths of the RWG section and DBR section had been optimized in previous processes to achieve single-mode operation in the lateral direction, and emission at a single frequency. No cavity spoiling elements were utilized in the tapered lasers, and the front and back facets were AR coated to achieve minimum reflectance at 1180 nm.

The lasers were mounted p-side down on AlN submounts, and the submounts were mounted on copper heatsinks to achieve effective heat dissipation, which is necessary for high-power operation. All of the laser components were planarized with benzocyclobutene (BCB). This also reduces the parasitic capacitance in the devices [38, p. 272].

4.2 Characterization methods

In order to calculate the brightness B of a laser component, the output power P, the emission wavelength λ_{peak}, and the M^2 factors need to be measured. In addition, the far field divergence angle θ needs to be known to choose an appropriate lens for collimating the laser beam. All the characterization methods used in the analysis are introduced in the following subsections.

4.2.1 LI measurement

LI (light output and current) measurement measures the output power P of a laser component as a function of drive current I. The component is driven with different I values, and simultaneously P is measured from the laser output.

In this thesis, P was measured with an integrating sphere, and a photodiode. In an integrating sphere, the input beam is diffused by the reflecting surfaces within the sphere, and after numerous reflections the radiation is distributed evenly throughout the sphere. A photodiode can then be used to measure a known fraction of the power of the laser beam. Figure 4.2 shows a schematic of an output power measurement with an integrating sphere.

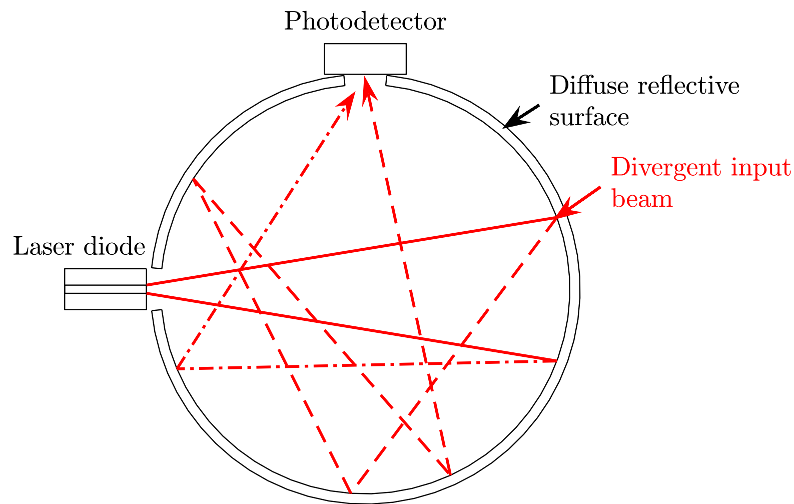

Figure 4.2 *A schematic of a laser diode output power measurement using an integrating sphere.*

An integrating sphere can collect most of the light that is emitted. This allows even highly diverging beams to be measured, and also reduces the variation in measurements that is caused by different beam shapes. Because only a small part of the beam hits the photodetector, an integrating sphere can measure high powers, but this also increases the minimum detectable power.

4.2.2 Spectrum and far field

The emission wavelength λ_{peak} can be determined by measuring the optical spectrum of the laser component. In this thesis, the spectrum was measured with a commercial

optical spectrum analyzer (OSA), and the λ_{peak} was defined as the wavelength value, which has the highest intensity.

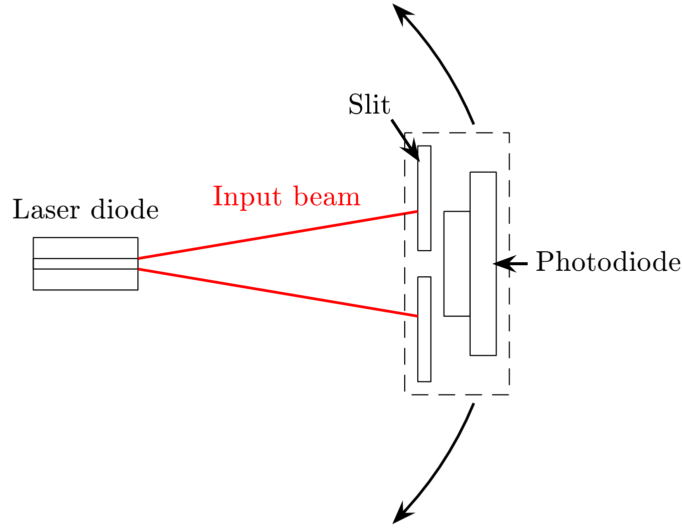

Figure 4.3 *A schematic of a laser diode far field measurement system.*

In order to calculate the far field divergence angle, the far field was also measured. Far field defines the output power P as a function of output angle θ_{out}. The horizontal and vertical far field was measured by placing a slit in front of a photodiode, and rotating the slit and photodiode together with respect to the output facet of the laser component. Figure 4.3 illustrates this type of a far field measurement system.

4.2.3 Beam quality measurement

The beam quality measurement setup used in this thesis is identical to the one shown in Figure 2.4. The RWG lasers were collimated with an aspheric lens, and the astigmatic beam of the tapered DBR lasers was collimated with two acylindrical lenses. The beam was focused with an achromatic doublet lens to reduce spherical aberration effects. The model, the effective focal length (EFL), and the NA of the lenses are shown in Table 4.4. All of the lenses were AR-coated to minimize any reflections at the emission wavelength of the lasers.

A movable corner mirror consisting of two silver mirrors was used to reflect the laser beam to the beam profiler. Scanning slit beam profiler was chosen as the beam profiling method, since only the beam radius is of importance, and because of its advantages over CCD and pyroelectric camera, that were explained in Subsection 2.4.3.

Table 4.4 *List of lenses that were used to collimate and focus the laser components.*

RWG laser collimation lens	LightPath 355330C, aspheric lens, EFL 3.10 mm, NA 0.77
Tapered laser collimation lens	**FA:** FISBA FAC 600, acylindrical lens, EFL 0.6 mm, NA 0.8 **SA:** Asphericon CHL18-15-S-U, acylindrical lens, EFL 15 mm, NA 0.53
Focusing lens	TECHSPEC Near-IR Achromatic Lens, achromatic doublet, EFL 200 mm, NA 0.06

Thorlabs BP209-IR/M dual scanning slit beam profiler was used to profile the beam. The profiler has an InGaAs photodetector, 9 mm aperture, and a slit width of 5 µm.

The collimated beam was first aligned in such way that it remained still at the beam profiler when the mirrors were moved. The focusing lens was then placed in front of the beam, and it was aligned such that the beam again remained in the same position when the mirrors were moved. The collimation lenses were then adjusted such that the beam was focused 200 mm away from the principal plane of the focusing lens.

The $D4\sigma$ method was used to calculate the beam radii in the FA and SA directions, which correspond to the principal axes of the beam. The beam radii were measured at 100 different distances with 2 mm spacing, and a nonlinear regression model was used to fit Equations (2.2.5) and (2.2.6) to the data to obtain a nonlinear function. The M^2 factors were then calculated from the obtained function.

5. RESULTS AND ANALYSIS

The measurement data for LI curves, spectra, far field and beam quality measurements are presented in this chapter. Using these results, the brightness is then calculated and analyzed for each laser component.

5.1 Measurement results

The measurement results and analysis for the RWG laser components and tapered laser components are presented in the following subsections. All of the measurements were performed at 20°C.

5.1.1 LI curves

The LI curves for the RWG lasers with symmetric and asymmetric structure are shown in Figures 5.1 and 5.2, respectively. The kinks that are present in the curves imply the excitation of higher-order modes or changes in material properties.

The LI curves for the tapered DBR lasers are shown in Figure 5.3. The maximum output powers obtained are much higher than for the RWG lasers as could be expected. However, the LI curves are not very linear, even at low drive currents. This implies the presence of higher-order modes, and possible nonlinear effects, such as self-focusing.

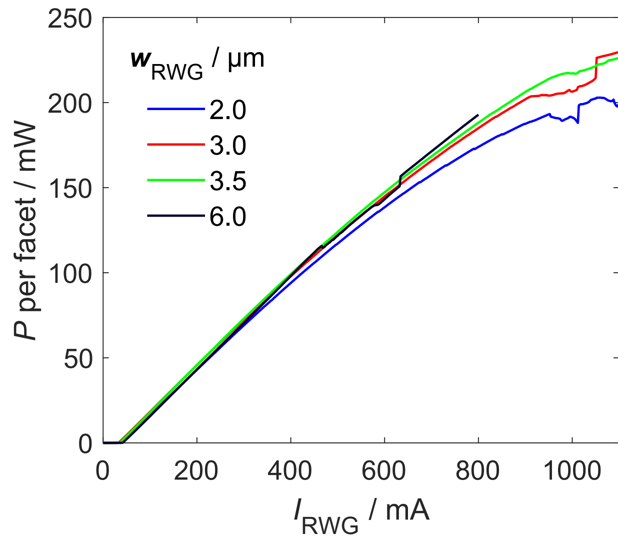

(a) RWG, sym. struct., t_{RWG} = 1120 nm

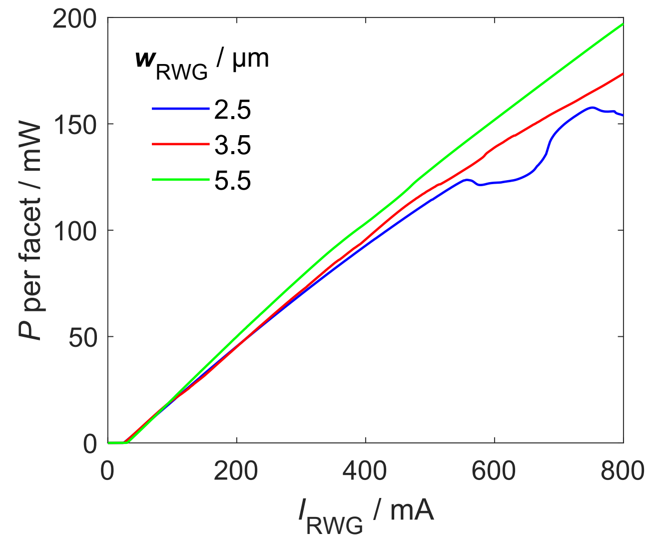

(b) RWG, sym. struct., t_{RWG} = 1270 nm

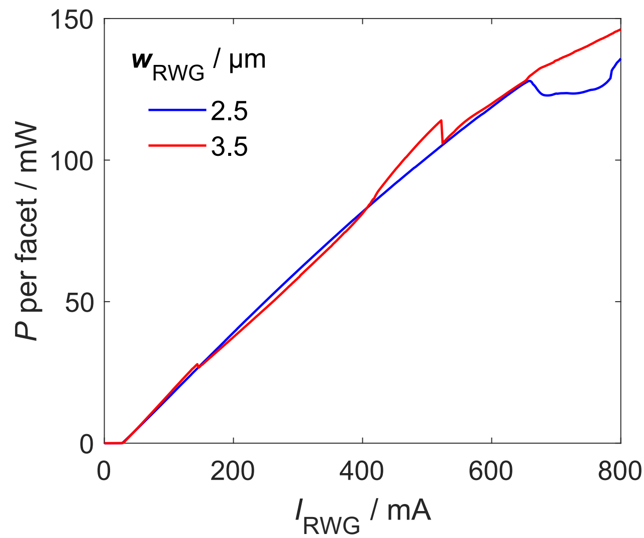

(c) RWG, sym. struct., t_{RWG} = 1300 nm

Figure 5.1 *The output power P_{out} per facet as a function of drive current I_{RWG} for the RWG laser components with symmetric structure.*

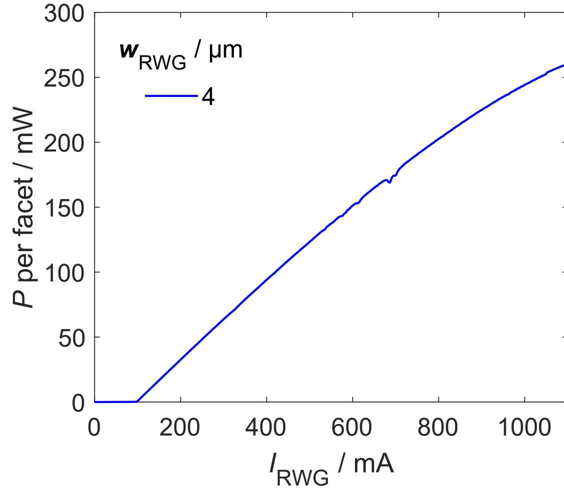

(a) RWG, asym. struct., t_{RWG} = 1280 nm

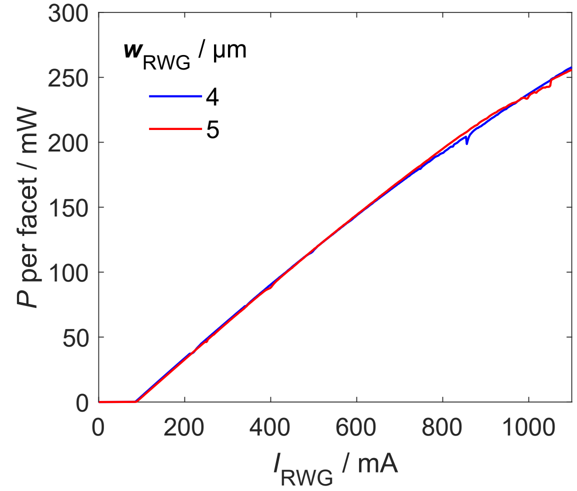

(b) RWG, asym. struct., t_{RWG} = 1580 nm

Figure 5.2 *The output power P_{out} per facet as a function of drive current I_{RWG} for the RWG laser components with asymmetric structure.*

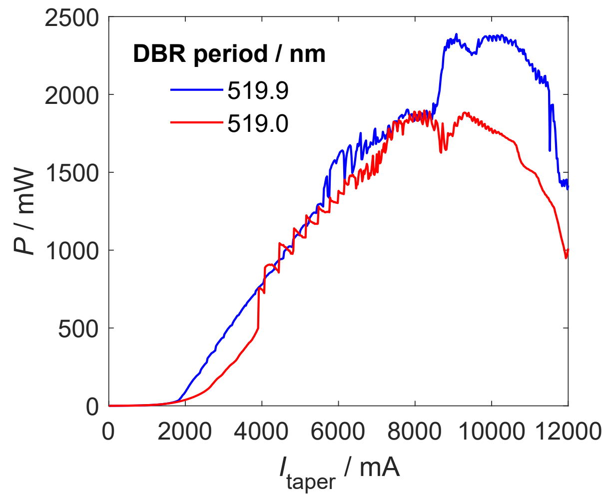

Figure 5.3 *The output power P_{out} as a function of drive current to the tapered section I_{taper} for the tapered DBR lasers. The drive current to the RWG section I_{RWG} was kept constant at 250 mA.*

5.1.2 Spectra and emission wavelengths

The spectra at two drive currents I_{RWG} for one of the symmetric structure RWG laser are shown in Figure 5.4. The spectra are relatively broad, with a FWHM of approximately 2.4 nm and 3.3 nm at drive currents I_{RWG} of 200 mA and 1100 mA, respectively. However, the error that this causes to the calculated M^2 factors is negligible (less than 0.01). The emission wavelength λ_{peak} as a function of drive current I_{RWG} for all the symmetric structure RWG lasers is shown in Figure 5.5. The λ_{peak} values are close to the target value of 1180 nm.

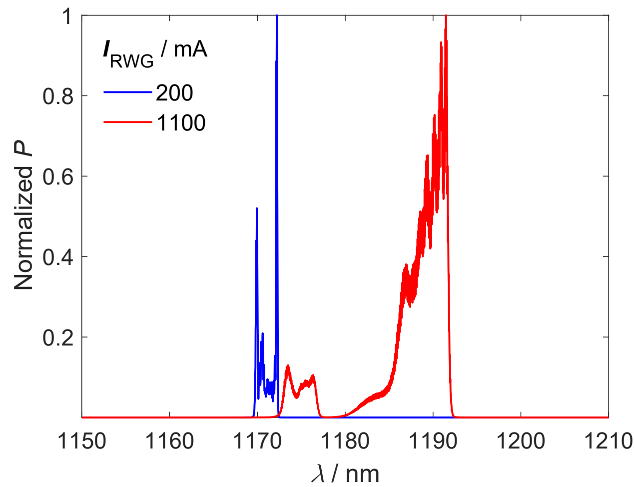

Figure 5.4 *The spectra at two drive currents I_{RWG} for the symmetric structure RWG laser with w_{RWG} of 3.5 µm and t_{RWG} of 1300 nm.*

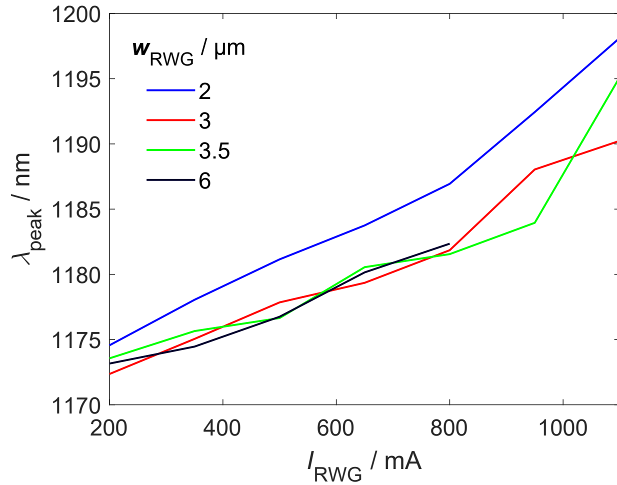

(a) RWG, sym. struct., t_{RWG} = 1120 nm

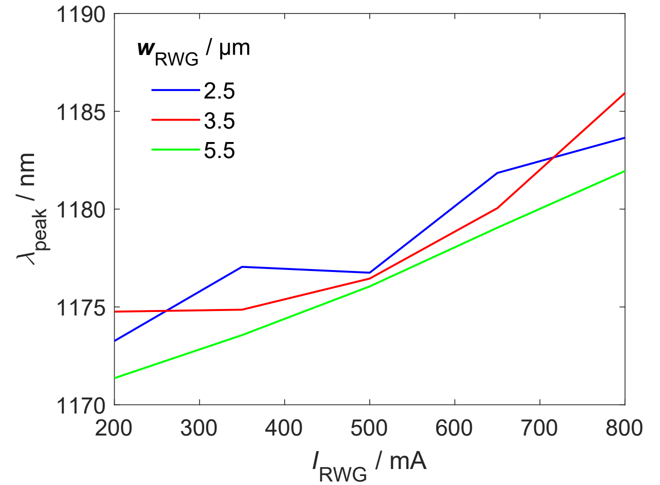

(b) RWG, sym. struct., t_{RWG} = 1270 nm

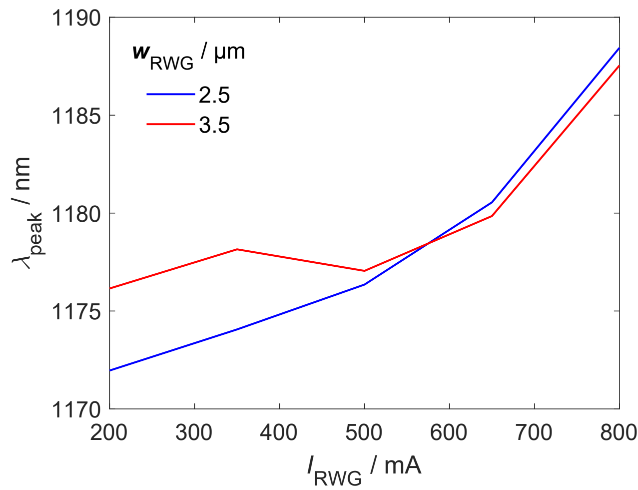

(c) RWG, sym. struct., t_{RWG} = 1300 nm

Figure 5.5 *The emission wavelength λ_{peak} as a function of drive current I_{RWG} for the RWG laser components with symmetric structure.*

The spectra at two drive currents I_{RWG} for one of the asymmetric structure RWG laser are shown in Figure 5.6. This time the spectra are much narrower, with a FWHM of approximately 0.1 nm and 1.3 nm at drive currents I_{RWG} of 200 mA and 1100 mA, respectively. The emission wavelength λ_{peak} as a function of drive current I_{RWG} for all the asymmetric structure RWG lasers is shown in Figure 5.7. The λ_{peak} values deviate around 20 nm from the target value of 1154 nm.

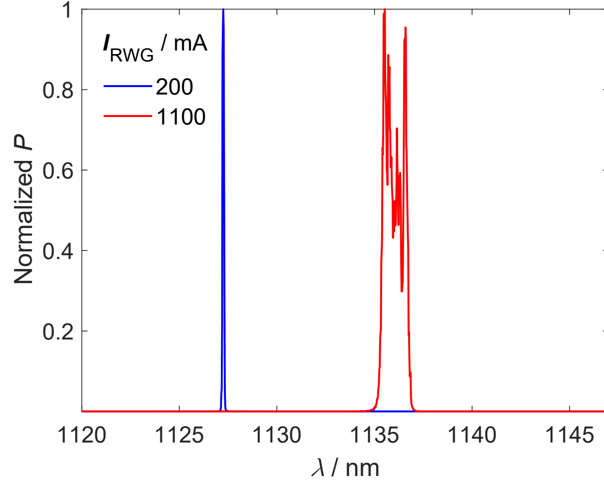

Figure 5.6 *The spectra at two drive currents I_{RWG} for the asymmetric structure RWG laser with w_{RWG} of 4.0 µm and t_{RWG} of 1580 nm.*

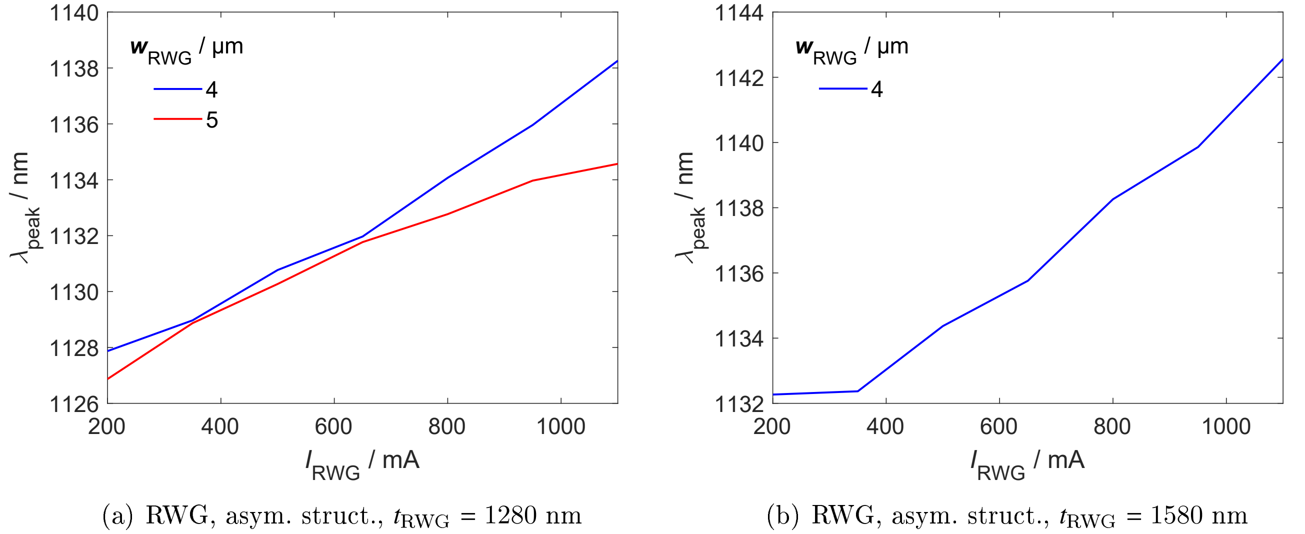

(a) RWG, asym. struct., t_{RWG} = 1280 nm (b) RWG, asym. struct., t_{RWG} = 1580 nm

Figure 5.7 *The emission wavelength λ_{peak} as a function of drive current I_{RWG} for the RWG laser components with asymmetric structure.*

The spectra at two drive currents I_{taper} with constant I_{RWG} for one of the tapered DBR lasers are shown in Figure 5.8. Due to the DBR, the spectra are very narrow, with a FWHM of approximately 0.1 nm at both drive currents I_{taper} of 4000 mA and 10000 mA. The emission wavelength λ_{peak} as a function of drive current I_{taper} for both tapered DBR lasers is shown in Figure 5.9. The λ_{peak} values are very close to the target value of 1180 nm.

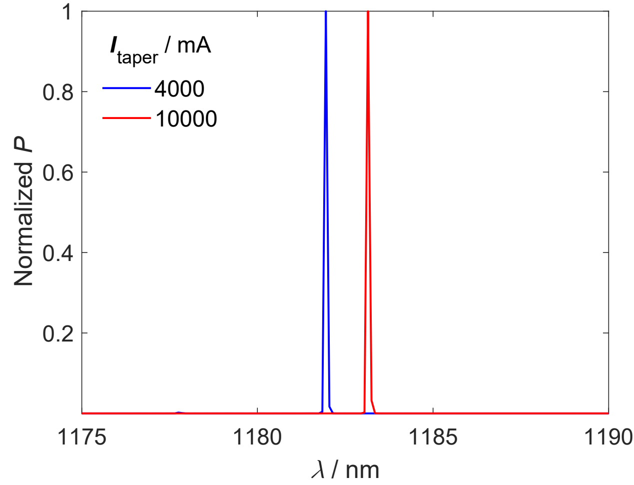

Figure 5.8 *The spectra at two drive currents I_{taper} for the tapered DBR laser with DBR period of 519.9 nm. The drive current to the RWG section I_{RWG} was kept constant at 250 mA.*

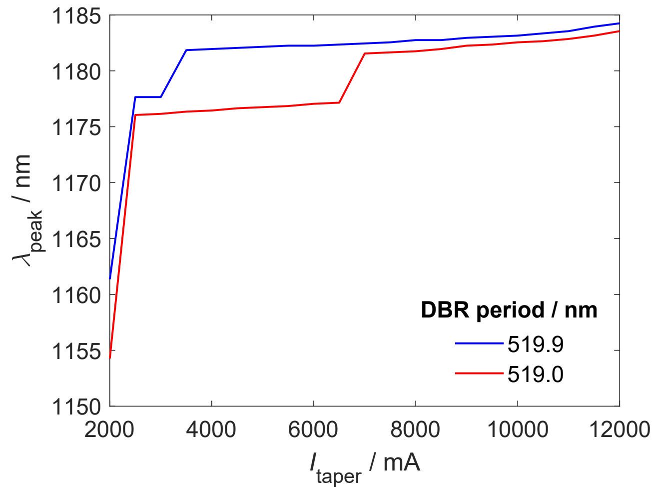

Figure 5.9 *The emission wavelength λ_{peak} as a function of drive current to the tapered section I_{taper} for the tapered DBR lasers. The drive current to the RWG section I_{RWG} was kept constant at 250 mA.*

To calculate the M^2 factors at drive currents for which spectrum data was missing, the emission wavelength data was linearly interpolated and extrapolated. The error that this causes to the calculated M^2 factors is again negligible.

5.1.3 Far field and numerical apertures

Figures 5.10 and 5.11 show the far fields at two drive currents I_{RWG} for two RWG laser components with symmetric and asymmetric structure, respectively. Some beam pointing instability is present in the SA direction when the drive current is changed in the RWG laser with symmetric structure, whereas the RWG laser with asymmetric structure remains very stable. The far field in the FA direction is narrower for the asymmetric structure due to thicker waveguide. Small shoulders in the beam become visible in the SA direction as the drive current is increased to 1100 mA, which suggests that there are some higher-order modes present.

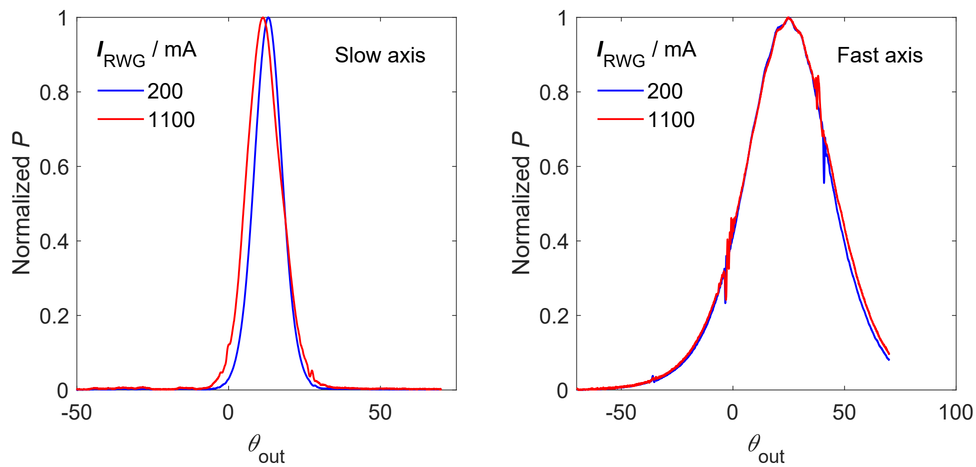

Figure 5.10 *The far field in the SA and FA directions at two drive currents I_{RWG} for the symmetric structure RWG laser with w_{RWG} of 3.5 µm and t_{RWG} of 1300 nm.*

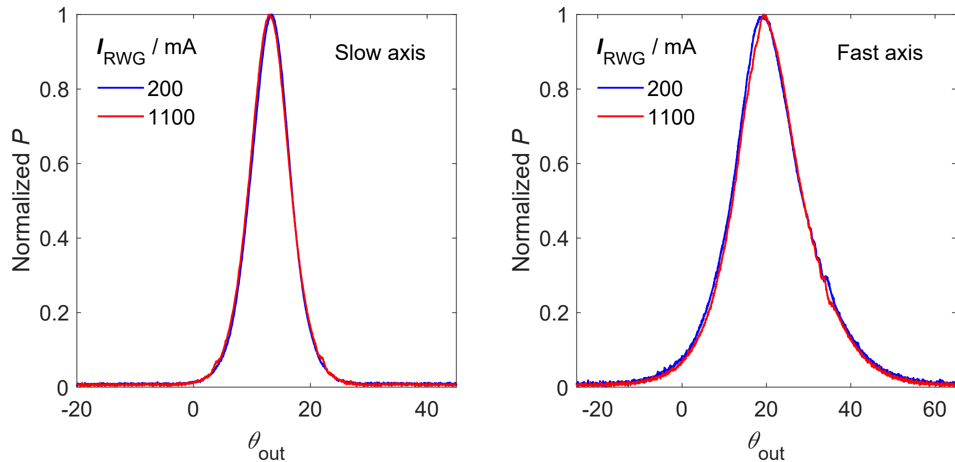

Figure 5.11 *The far field in the SA and FA directions at two drive currents I_{RWG} for the asymmetric structure RWG laser with w_{RWG} of 4.0 µm and t_{RWG} of 1580 nm.*

Figure 5.12 shows the far fields of the tapered DBR laser components at two drive currents I_{taper}, with constant I_{RWG}. Higher order modes, as well as possible self-focusing and filamentation effects are visible in the far field in the SA direction, even at the lower drive current. In addition, the shape of the far field in the FA direction does not stay unchanged as the drive current is changed.

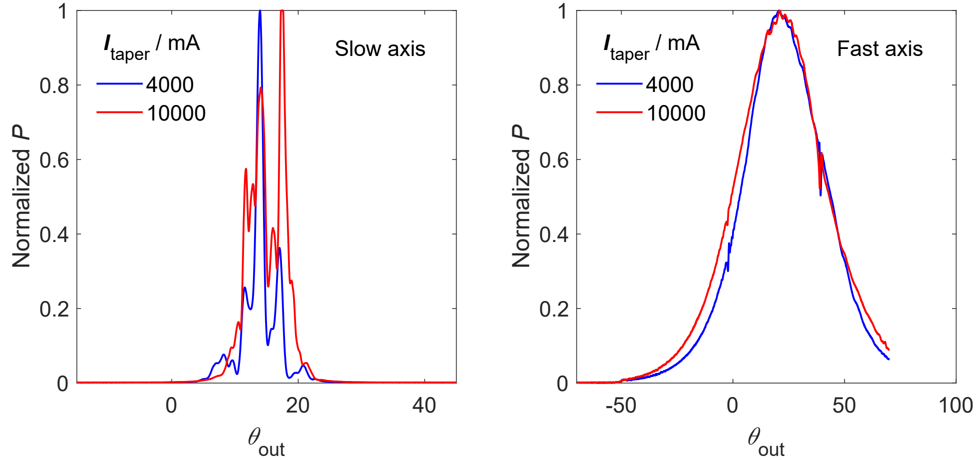

Figure 5.12 *The far field in the SA and FA directions at two drive currents I_{taper} for the tapered DBR laser with DBR period of 519.9 nm. The drive current to the RWG section I_{RWG} was kept constant at 250 mA.*

Using the far field data from all the samples, the average divergence half-angles containing 95% of the beam power were calculated. From the divergence angles, the NAs were calculated using Equation (2.4.1). The divergence angles and NAs, and their respective standard deviations are shown in Table 5.1 for all laser types.

Table 5.1 *The average divergence angles $\theta_{95\%}$ containing 95% of the output power, and the corresponding average NA values, together with the standard deviations, for all the three laser types.*

Laser type	$\theta_{95\%}$		$\mathbf{NA}_{95\%}$	
	SA	FA	SA	FA
RWG, sym. struct.	9.71° ± 3.00°	42.02° ± 1.29°	0.17 ± 0.06	0.67 ± 0.02
RWG, asym. struct.	6.25° ± 1.41°	18.20° ± 1.24°	0.11 ± 0.03	0.31 ± 0.03
Tapered DBR, sym. struct	7.27° ± 0.76°	42.57° ± 1.89°	0.13 ± 0.02	0.68 ± 0.03

Comparing the NA values in Table 5.1 to the NA values of the lenses that were used to collimate the laser beams (see Table 4.4), the collimation lenses are able to collect over 95% of the beam power in both the SA and the FA direction. Thus, the obtained M^2 factors should be quite close to the actual M^2 factors of the lasers.

5.1.4 Beam profiles and M^2 factors

Figures 5.13 and 5.14 show the beam profiles for one of the symmetric RWG lasers at the beam waist, and in the far-field region, at two drive currents I_{RWG}. For comparison, a Gaussian beam with the same $D4\sigma$ width, and the same beam centroid as the beam at the drive current I_{RWG} = 200 mA is drawn in all the figures. Small shoulders in the beam wings are visible in the profiles, and the profiles are not completely symmetric. Especially the FA profiles deviate quite substantially from a Gaussian profile.

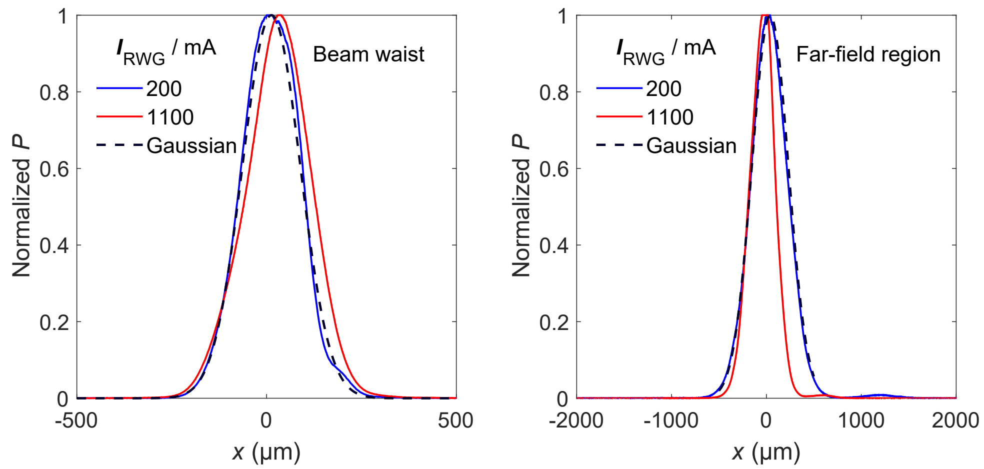

Figure 5.13 *The SA beam profile at beam waist, and in the far-field region at two drive currents I_{RWG} for the symmetric structure RWG laser with w_{RWG} of 3.5 µm and t_{RWG} of 1300 nm. A Gaussian beam with the same $D4\sigma$ width, and the same beam centroid as the beam at the drive current I_{RWG} = 200 mA is included as a reference.*

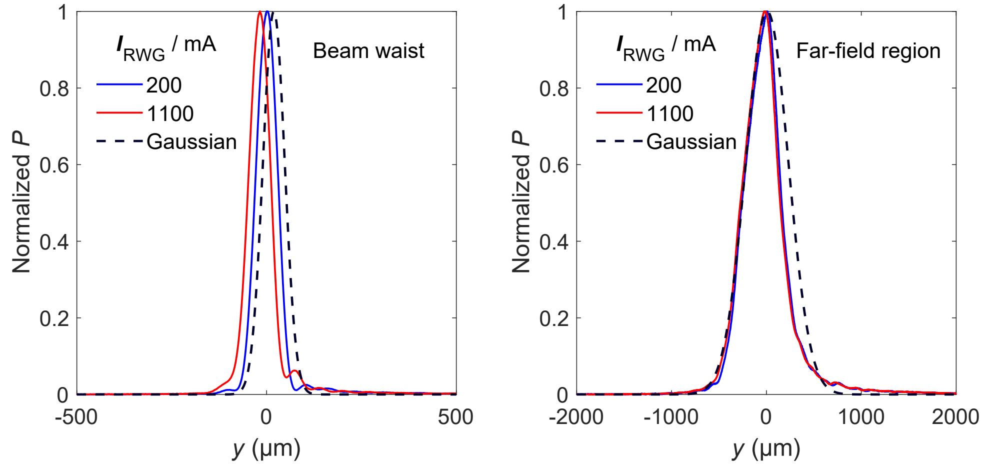

Figure 5.14 *The FA beam profile at beam waist, and in the far-field region at two drive currents I_{RWG} for the symmetric structure RWG laser with w_{RWG} of 3.5 µm and t_{RWG} of 1300 nm. A Gaussian beam with the same $D4\sigma$ width, and the same beam centroid as the beam at the drive current I_{RWG} = 200 mA is included as a reference.*

Figures 5.15 and 5.16 show the beam profiles for one asymmetric RWG laser at the beam waist, and in the far-field region, at two drive currents I_{RWG}. For comparison, a Gaussian beam with the same $D4\sigma$ width, and the same beam centroid as the beam at the drive current I_{RWG} = 200 mA is drawn in all the figures. Here the SA beam profile is closer to a Gaussian, although a small shoulder becomes visible at the higher drive current. The FA beam profile is still asymmetric, and displays a strange shape at the beam waist.

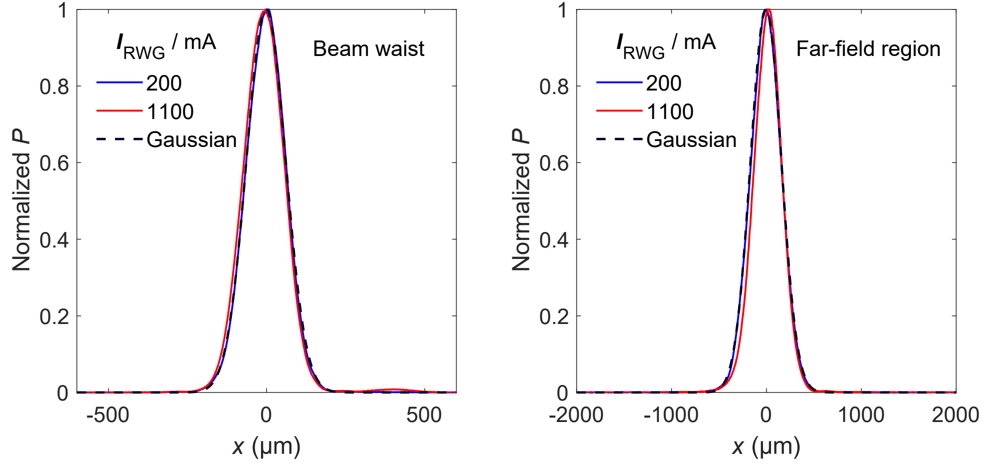

Figure 5.15 *The SA beam profile at beam waist, and in the far-field region at two drive currents I_{RWG} for the asymmetric structure RWG laser with w_{RWG} of 4.0 µm and t_{RWG} of 1580 nm. A Gaussian beam with the same $D4\sigma$ width, and the same beam centroid as the beam at the drive current I_{RWG} = 200 mA is included as a reference.*

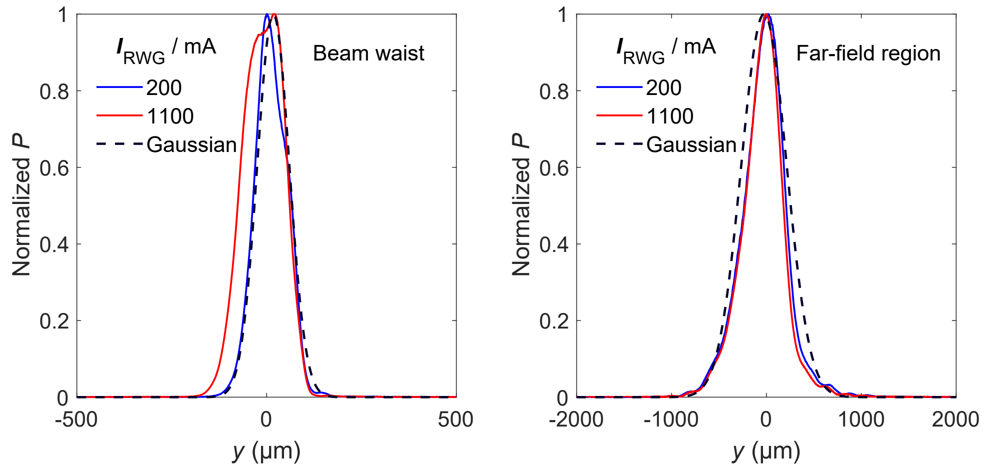

Figure 5.16 *The FA beam profile at beam waist, and in the far-field region at two drive currents I_{RWG} for the asymmetric structure RWG laser with w_{RWG} of 4.0 µm and t_{RWG} of 1580 nm. A Gaussian beam with the same $D4\sigma$ width, and the same beam centroid as the beam at the drive current I_{RWG} = 200 mA is included as a reference.*

Figures 5.17 and 5.18 show the beam profiles for one tapered DBR laser at the beam waist, and in the far-field region, at two drive currents I_{taper}, with constant I_{RWG}. For comparison, a Gaussian beam with the same $D4\sigma$ width, and the same beam centroid as the beam at the drive current I_{taper} = 4000 mA is drawn in all the figures. The SA beam profiles deviate significantly from a Gaussian profile, and they display

multiple peaks even at the lower drive current at the beam waist. This implies that the tapered DBR laser parameters are not optimal, and instead the tapered section of the lasers allows the propagation of higher order modes. The FA beam profiles deviate considerably from a Gaussian profile, as well.

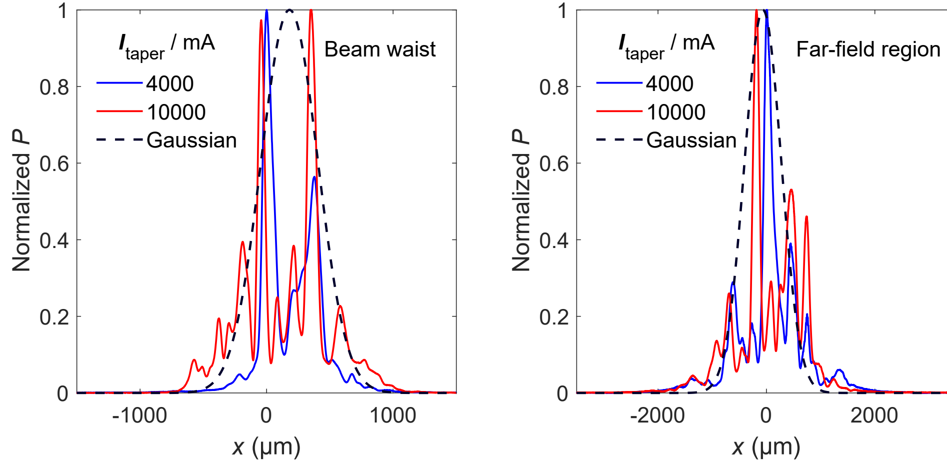

Figure 5.17 *The SA beam profile at beam waist, and in the far-field region at two drive currents I_{taper} for the tapered DBR laser with DBR period of 519.9 nm. The drive current to the RWG section I_{RWG} was kept constant at 250 mA. A Gaussian beam with the same D4σ width, and the same beam centroid as the beam at the drive current I_{RWG} = 4000 mA is included as a reference.*

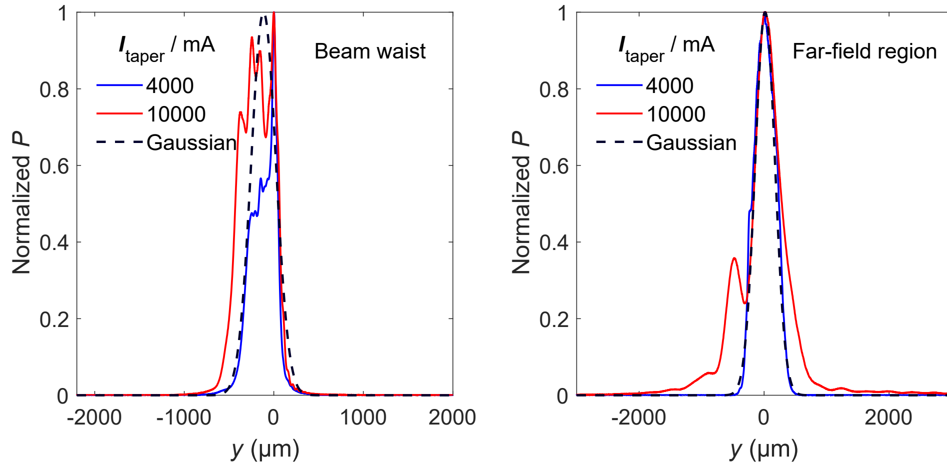

Figure 5.18 *The FA beam profile at beam waist, and in the far-field region at two drive currents I_{taper} for the tapered DBR laser with DBR period of 519.9 nm. The drive current to the RWG section I_{RWG} was kept constant at 250 mA. A Gaussian beam with the same D4σ width, and the same beam centroid as the beam at the drive current I_{RWG} = 4000 mA is included as a reference.*

The M^2 factors were calculated as a function of drive current using the emission wavelength data. The results with error bars for the RWG lasers with symmetric and asymmetric structure are shown in Figures 5.19–5.20 and Figures 5.21–5.22, respectively. All of the M^2 factors are relatively close to one, and the general trend is that narrower w_{RWG} values lead to better beam quality, which is due to the fact that they provide stronger index-guiding. The M^2 factors in the FA direction M^2_{FA} are higher than the ones in the SA direction M^2_{SA}. This may be attributed to the epitaxial structure, or it may also be caused by the lenses, which might introduce some spherical aberration to the beam, due to large divergence and large beam size in the FA direction. Looking at Figure 5.20, the beam quality factor M^2_{FA} reaches a value below one for the laser with ridge width $w_{\mathrm{RWG}} = 3.0$ µm and etch depth $t_{\mathrm{RWG}} = 1120$ nm. Since this is physically not possible, this data point will be omitted from the brightness analysis.

The RWG lasers with asymmetric structure have better M^2 factors in the FA direction, which may be attributed to less spherical aberration introduced by the collimation lens, due to lower divergence compared to the symmetric structure. The M^2 factors in the SA direction are also smaller, which maybe due to deeper etch depth leading to stronger index-guiding, different epitaxial structure, a more successful laser processing, or a combination of these factors. In addition, the asymmetric RWG lasers have much more stable M^2 factors, that stay relatively constant as the drive current is increased. The asymmetric RWG laser with ridge width of 4.0 µm at etch depth of 1580 nm shows the lowest and the most stable M^2 factors.

The errors of the M^2 factors in the FA direction for the RWG lasers with symmetric structure are large due to the fact that only a small fraction of the measurement points are within the narrow Rayleigh range. This could be improved by measuring more points within the Rayleigh range, and by focusing the beam further away from the lens.

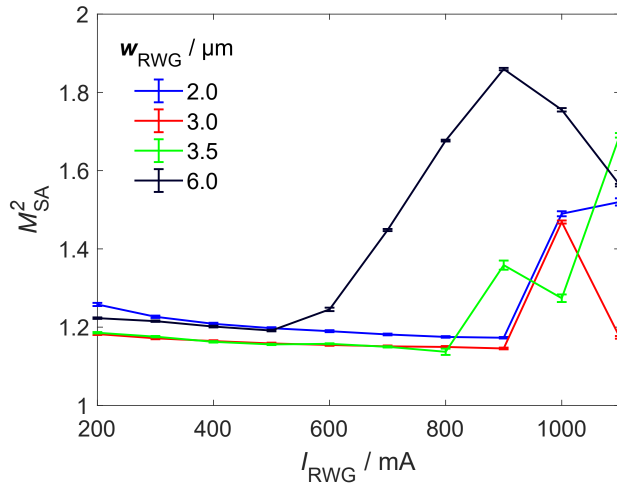

(a) RWG, sym. struct., t_{RWG} = 1120 nm

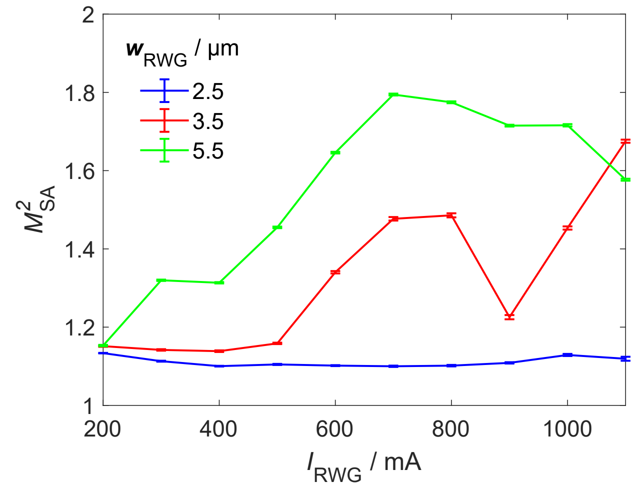

(b) RWG, sym. struct., t_{RWG} = 1270 nm

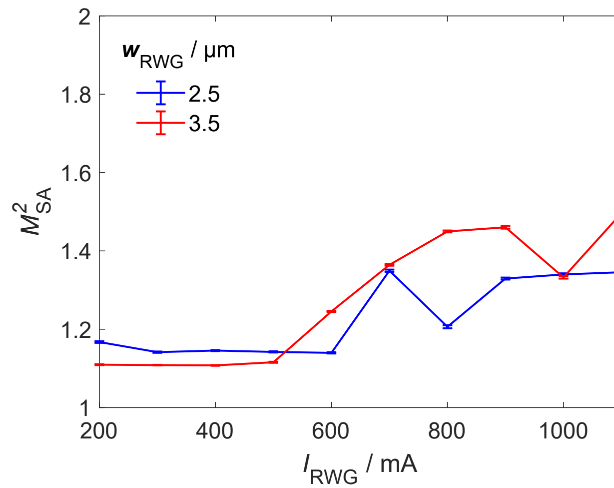

(c) RWG, sym. struct., t_{RWG} = 1300 nm

Figure 5.19 *The beam quality factor in the SA direction M^2_{SA} as a function of drive current I_{RWG} for the RWG laser components with symmetric structure.*

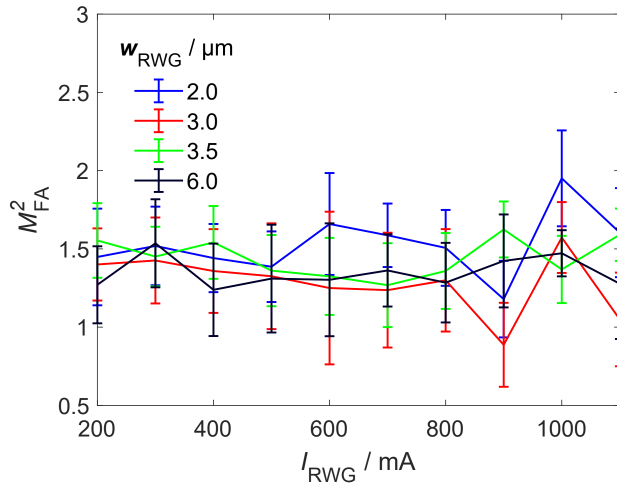

(a) RWG, sym. struct., t_{RWG} = 1120 nm

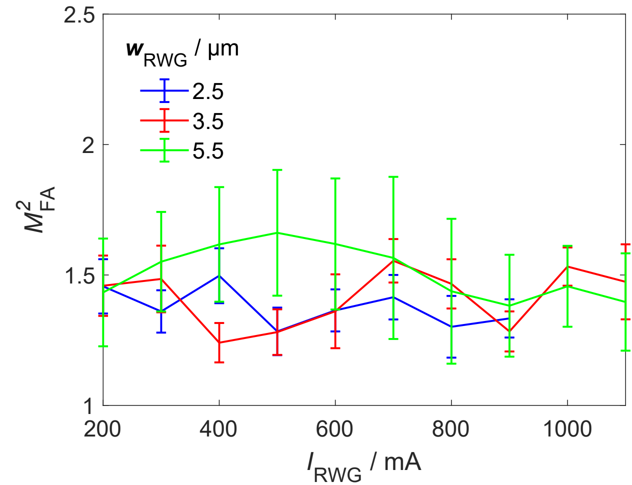

(b) RWG, sym. struct., t_{RWG} = 1270 nm

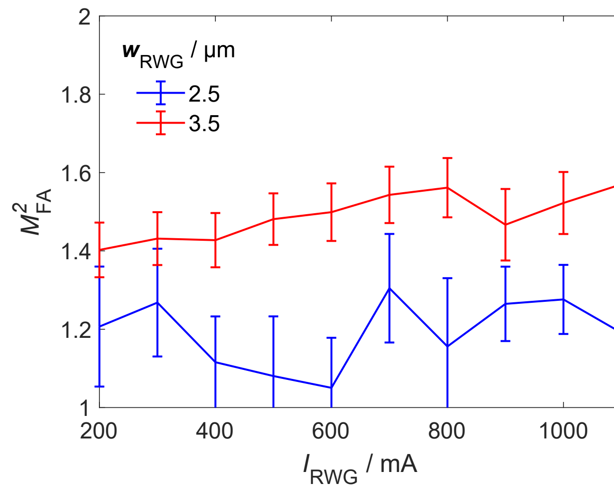

(c) RWG, sym. struct., t_{RWG} = 1300 nm

Figure 5.20 *The beam quality factor in the FA direction M^2_{FA} as a function of drive current I_{RWG} for the RWG laser components with symmetric structure.*

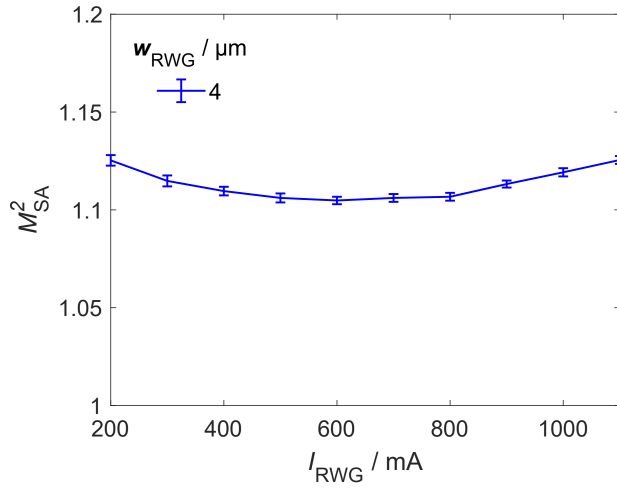

(a) RWG, asym. struct., t_{RWG} = 1280 nm

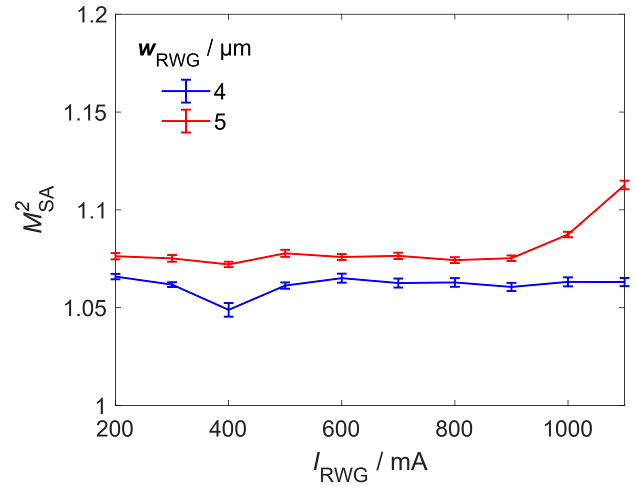

(b) RWG, asym. struct., t_{RWG} = 1580 nm

Figure 5.21 *The beam quality factor in the SA direction M^2_{SA} as a function of drive current I_{RWG} for the RWG laser components with asymmetric structure.*

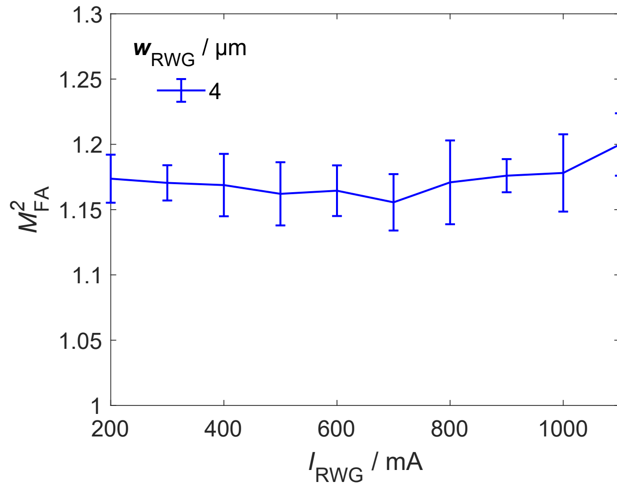

(a) RWG, asym. struct., t_{RWG} = 1280 nm

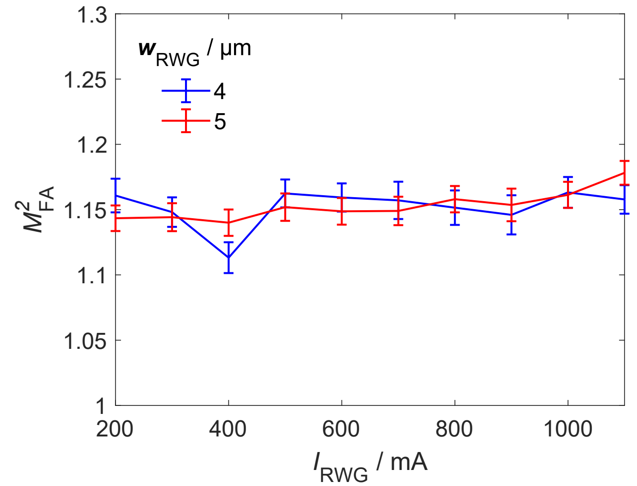

(b) RWG, asym. struct., t_{RWG} = 1580 nm

Figure 5.22 *The beam quality factor in the FA direction M^2_{FA} as a function of drive current I_{RWG} for the RWG laser components with asymmetric structure.*

The results for the tapered DBR lasers are shown in Figures 5.23 and 5.24. Both laser components have poor M^2 factors in both the SA and FA directions. The poor M^2 factors most likely caused by higher-order modes and possible self-focusing and filamentation. The component with DBR period of 519.9 nm has a lower M^2 factor at low drive currents, while the component with DBR period of 519.0 nm has a lower M^2 factor at the highest drive currents. The M^2 factors are similar at the drive currents in the middle.

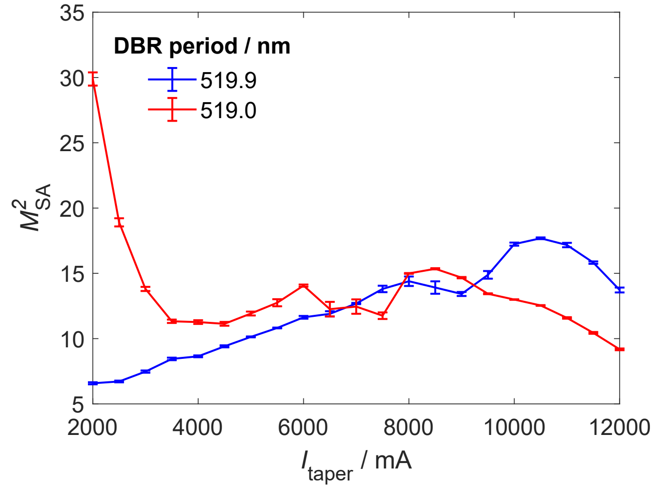

Figure 5.23 *The beam quality factor in the SA direction M^2_{SA} as a function of drive current to the tapered section I_{taper} for the tapered DBR lasers. The drive current to the RWG section I_{RWG} was kept constant at 250 mA.*

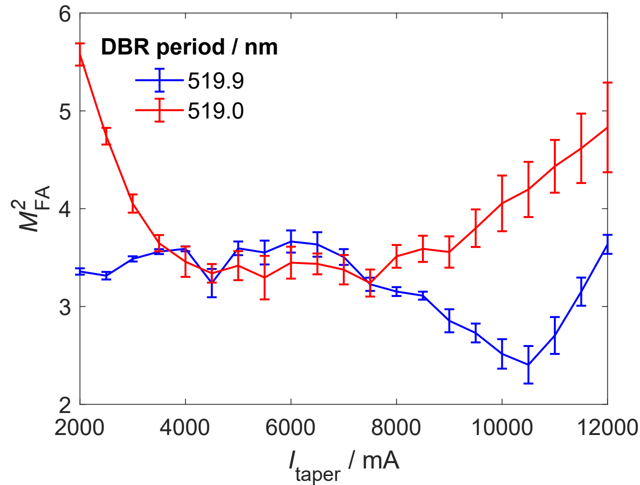

Figure 5.24 *The beam quality factor in the FA direction M^2_{FA} as a function of drive current to the tapered section I_{taper} for the tapered DBR lasers. The drive current to the RWG section I_{RWG} was kept constant at 250 mA.*

5.2 Brightness analysis

Using the output powers P, emission wavelengths λ_{peak}, and M^2 factors obtained from the measurements, the brightness B as a function of drive current I was calculated for each laser component, utilizing Equation (2.3.5). The results for the symmetric and asymmetric structure RWG laser components are shown in Figures 5.25 and 5.26, respectively, and the results for the tapered DBR laser components are shown in Figure 5.27.

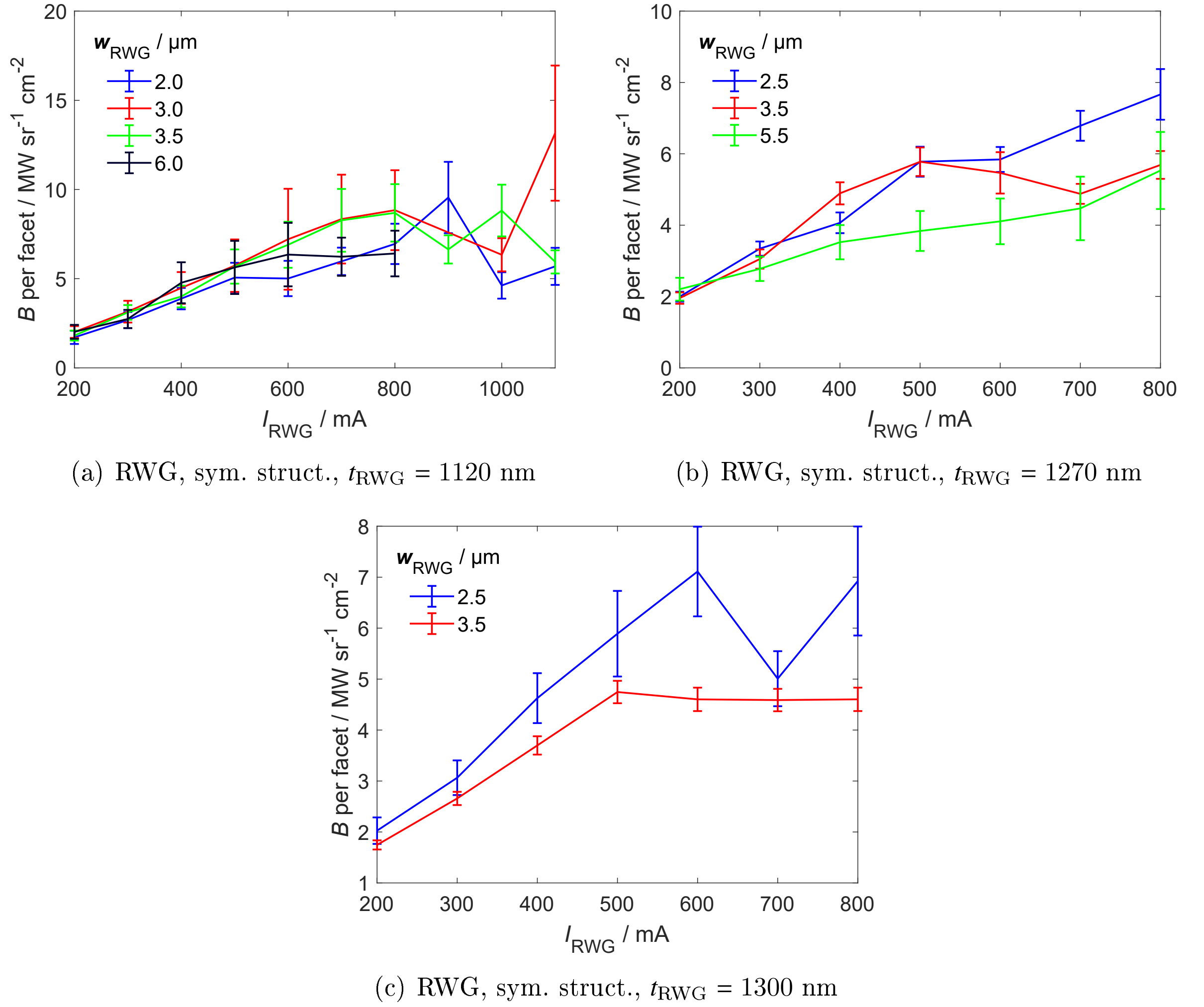

(a) RWG, sym. struct., t_{RWG} = 1120 nm

(b) RWG, sym. struct., t_{RWG} = 1270 nm

(c) RWG, sym. struct., t_{RWG} = 1300 nm

Figure 5.25 *The laser brightness B as a function of drive current I_{RWG} for the RWG laser components with symmetric structure.*

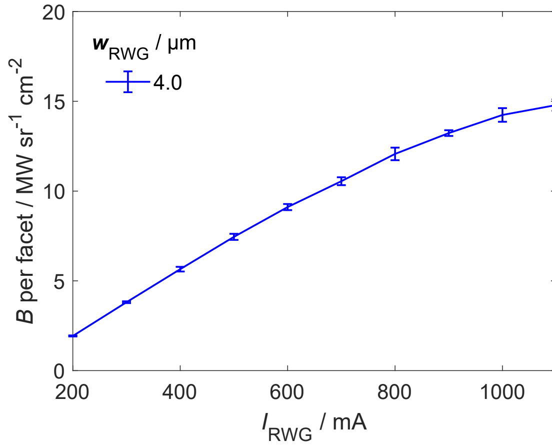

(a) RWG, asym. struct., t_{RWG} = 1280 nm

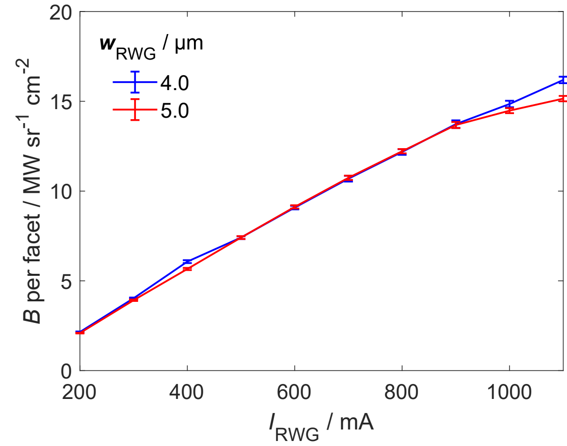

(b) RWG, asym. struct., t_{RWG} = 1580 nm

Figure 5.26 *The laser brightness B as a function of drive current I_{RWG} for the RWG laser components with asymmetric structure.*

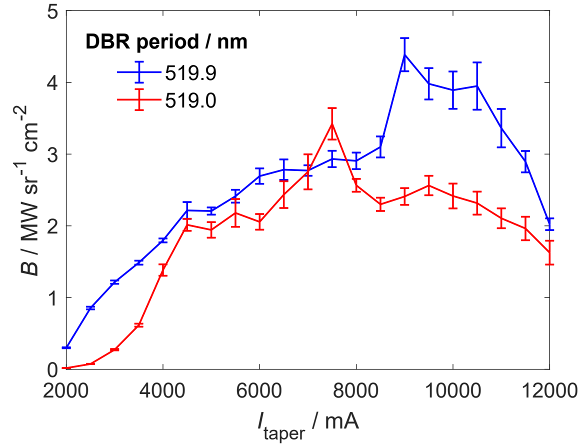

Figure 5.27 *The laser brightness B as a function of drive current to the tapered section I_{taper} for the tapered DBR lasers. The drive current to the RWG section I_{RWG} was kept constant at 250 mA.*

Based on the results, the highest brightness values for the symmetric structure RWG lasers are obtained at the most shallow etch depth of 1120 nm. The brightnesses seem to saturate at the high current values, and the highest brightness of 13.16 ± 3.79 MW sr^{-1} cm^{-2} was measured for the ridge width of 3.0 µm at a drive current of 1100 mA.

The asymmetric RWG lasers display much more stable, almost linear behavior. The highest brightness values are obtained at the deepest etch depth of 1580 nm. The

highest brightness of 16.19 ± 0.18 MW sr^{-1} cm^{-2} was measured for the ridge width of 4.0 µm at a drive current of 1100 mA. Based on the trend, higher brightness values may be achievable at higher drive currents.

While the tapered DBR lasers had the highest output power, they display the poorest brightness values due to the poor M^2 factors. The brightness saturates at the high drive currents, and the highest brightness of 4.39 ± 0.24 MW sr^{-1} cm^{-2} is obtained at drive current of 9000 mA for the laser component with DBR period of 519.9 nm. The maximum brightness values that were measured for each laser type are summarized in Table 5.2.

Table 5.2 *The maximum brightness values B_{max} achieved, and the corresponding laser parameters for each of the three laser types. The error values originate from the error in the M^2 factors.*

Laser type	**Laser parameters**	**B_{max} / MW sr^{-1} cm^{-2}**
RWG, sym. struct.	w_{RWG} = 3.0 µm, t_{RWG} = 1120 nm	13.16 ± 3.79
RWG, asym. struct.	w_{RWG} = 4.0 µm, t_{RWG} = 1580 nm	16.19 ± 0.18
Tapered DBR, sym struct.	DBR period: 519.9 nm	4.39 ± 0.24

The poor brightness of the tapered DBR laser components is most likely related to the unoptimized design parameters, which lead to poor beam quality. The symmetric structure RWG laser with w_{RWG} of 3.5 µm, and t_{RWG} of 1300 nm is the closest to the RWG of the tapered DBR lasers. Its far-field divergence angle is around 7.6°. Assuming that the effective refractive index of the symmetric RWG structure is 3.5, the free diffraction angle in the tapered region would be around 2.2°, which is much smaller than the opening angle θ_{taper} = 5° that was used. This means that the overlap of the tapered region with the optical field is poor. This inevitably leads to the presence of higher-order modes, because the system has a large amount of gain unavailable to the fundamental mode.

The poor beam quality in the FA direction in the tapered DBR lasers may partly be explained by the fact that the acylindrical lens, that was used to collimate the beam in the FA direction, was not properly aligned. The adjustment of the lens was done manually by differential adjusters. In addition, the lens may not be entirely aberration-free at large angles, which might degrade the M^2 factor. There might be some kind of issue with the AR coating of the lens, as well. On the other hand, the FA collimation was also attempted with the aspheric lens that was used to collimate

the RWG laser components, but there was no improvement in the obtained M^2 factor. In fact, slightly larger M^2 factors were obtained in the FA direction.

One way to confirm that the FA collimation lens works as it should, would be to perform an M^2 factor measurement on one of the RWG lasers that had good beam quality, by using the acylindrical lenses to collimate the SA and FA directions. If the obtained M^2 factors were to be higher than the M^2 factors that were obtained with the aspheric lens, it would imply that there is a problem with the acylindrical lenses.

6. SUMMARY

This chapter summarizes the work that was done, the measurements that were made, and the results that were obtained. Future prospects together with further measurements and possible improvements that could be made are also suggested.

6.1 Conclusions

The aim of this thesis was to measure and analyze the brightness of edge-emitting lasers. Two types of lasers were analyzed: RWG lasers and tapered DBR lasers. For the RWG lasers, the goal was to determine the optimum etch depth and ridge width that lead to the highest brightness. Two types of RWG lasers were analyzed, ones with a symmetric epitaxial structure and ones with an asymmetric epitaxial structure. For the tapered DBR lasers, two laser components with different DBR periods were analyzed, and the goal was to determine if there is an improvement in the brightness compare to the RWG lasers. The tapered DBR lasers had a symmetric epitaxial structure.

The brightness was calculated by measuring the LI curves to determine the output power, measuring the spectrum to determine the emission wavelength, and perform beam divergence measurements to determine the M^2 factors. All of these were then used to calculate the brightness as a function of drive current.

The RWG lasers that had an asymmetric epitaxial structure displayed much stabler performance compared to the symmetric ones, with fewer kinks in the LI curves, stabler and lower M^2 factors in both the SA direction and the FA direction. The better beam quality in the FA direction may be due to different epitaxial structure or due to the fact that the FA divergence is narrower, and the beam radius in FA direction is smaller, which means that the possible spherical aberrations introduced by the lenses is smaller. The better beam quality in the SA direction may be due to different epitaxial structure or due to the fact that the process was more successful.

Summary of the results for the RWG lasers that achieved the highest brightness is shown in Table 6.1. Higher brightness values were achieved with the asymmetric structure, due to the improved beam quality in both the SA and FA directions. The highest brightness that was achieved with the asymmetric structure RWG lasers was 16.19 ± 0.18 MW sr^{-1} cm^{-2}, with a ridge width of 4.0 µm, and an etch depth of 1580 nm, at a drive current of 1100 mA. In comparison, for the symmetric structure RWG lasers, the highest brightness that was calculated was 13.16 ± 3.79 MW sr^{-1} cm^{-2}, with a ridge width of 3.0 µm, and an etch depth of 1120 nm, at a drive current of 1100 mA. Thus, an asymmetric epitaxial structure seems to be beneficial when trying to maximize the brightness of a laser.

Table 6.1 *Summary of all the variables that lead to the maximum brightness value for the RWG lasers, together with the output power and beam quality factors. The error values originate from the error in the M^2 factors.*

Laser type	**Ridge width / µm**	**Etch depth / nm**	**Drive current / mA**	**Output power / mW**	**Beam quality factors**	**Maximum brightness / MW sr^{-1} cm^{-2}**
RWG, sym. struct.	3.0	1120	1100	229	$M^2_{SA} \approx 1.17 \pm 0.01$, $M^2_{FA} \approx 1.05 \pm 0.30$	13.16 ± 3.79
RWG, asym. struct.	4.0	1580	1100	258	$M^2_{SA} \approx 1.06 \pm 0.01$, $M^2_{FA} \approx 1.16 \pm 0.01$	16.19 ± 0.18

Table 6.2 *Summary of all the variables that lead to the maximum brightness value for the tapered DBR lasers, together with the output power and beam quality factors. The error values originate from the error in the M^2 factors.*

Laser type	**DBR period / nm**	**Drive current / mA**	**Output power / W**	**Beam quality factors**	**Maximum brightness / MW sr^{-1} cm^{-2}**
Tapered DBR, sym. struct.	519.9	9000	2.35	$M^2_{SA} \approx 13.42 \pm 0.16$, $M^2_{FA} \approx 2.85 \pm 0.12$	4.39 ± 0.24

Summary of the results for the tapered DBR laser that achieved the highest brightness is shown in Table 6.2. The tapered DBR lasers achieved much higher output power compared to the RWG lasers, with a maximum output power of approximately 2.39 W achieved at a drive current of 9080 mA for the laser with a DBR period of 519.9 nm. However, the beam quality was poor in both the SA direction and the FA direction, due to the presence of higher order modes, even at low drive currents. Because of the poor beam quality, the maximum output brightness that was achieved was only 4.39 ± 0.24 MW sr^{-1} cm^{-2}, which was measured at a drive current

of 9000 mA for the laser component with a DBR period of 519.9 nm. This is much smaller than the brightness values that were achieved for the RWG lasers. Brightnesses as high as 800 MW sr^{-1} cm^{-2}, emitting at a wavelength of 1060 nm have been reported in the literature [37], which implies that the design of the tapered DBR lasers measured here is not optimal. The low brightness can mainly be attributed to the too wide opening angle of the tapered section, which allows the propagation of higher order modes.

6.2 Future prospects

The RWG lasers with an asymmetric structure showed superior behavior in terms of stability, beam quality and brightness, compared to the symmetric structure RWG lasers. However, the amount of asymmetric RWG lasers components that were analyzed was very small. In order to find the most optimum design parameters, a much wider variety of different RWG width and etch depth combinations need to be analyzed. The lifetime of the RWG lasers could also be measured to see how the symmetric and asymmetric structure compare in terms of reliability.

The tapered DBR lasers displayed poor brightness due to poor beam quality. The poor beam quality in the SA direction is likely due to unoptimized design parameters, such as the opening angle of the tapered section, which may be too large. An extensive analysis of tapered laser components with different design parameters should be performed in order to find the most optimal parameters that lead to the highest brightness. In order to further improve the beam quality, an asymmetric epitaxial structure similar to the one used in this thesis could be used, as it was found to lead to improved beam quality in both the SA and FA directions. This would also make it easier to collimate the beam in the FA direction, since the divergence angle would be narrower.

BIBLIOGRAPHY

[1] "Background Information on CCD and CMOS Technology," https://www.tedpella.com/cameras_html/ccd_cmos.htm, Accessed: 2018-09-05.

[2] "Beam Width Measurement Accuracy," https://www.ophiropt.com/laser--measurement/knowledge-center/article/8117, Accessed: 2018-06-27.

[3] "Camera Based Beam Profiling with BeamGage," https://www.ophiropt.com/laser--measurement/beam-profilers/products/Beam-Profiling/Camera-Profiling-with-BeamGage, Accessed: 2018-06-27.

[4] "Camera Basics," https://www.thorlabs.com/newgrouppage9.cfm?objectgroup_id=8962, Accessed: 2018-06-27.

[5] "Camera Noise and Temperature," https://www.thorlabs.com/newgrouppage9.cfm?objectgroup_id=10773, Accessed: 2018-06-27.

[6] "Pyroelectric Detectors Introduction," https://www.infratec.de/fileadmin/downloads/pdf/pyroelectric_detectors_introduction.pdf, Accessed: 2018-06-27.

[7] "Scanning Slit Beam Profiler with NanoScan," https://www.ophiropt.com/laser--measurement/beam-profilers/products/Scanning-Slit-Beam-Profiling-with-NanoScan, Accessed: 2018-06-27.

[8] "Tutorial: Pyroelectric Technology in Laser Sensors and Beam Analyzers," https://www.ophiropt.com/laser-measurement-instruments/beam-profilers/knowledge-center/tutorial/pyroelectric-technology, Accessed: 2018-06-27.

[9] "Lasers And Laser-Related Equipment—Test Methods For Laser Beam Widths, Divergence Angles And Beam Propagation Ratios—Part 2: General Astigmatic Beams," International Organization for Standardization, Geneva, Switzerland, ISO 11146-2:2005, 2005.

[10] "Lasers And Laser-Related Equipment—Test Methods For Laser Beam Widths, Divergence Angles And Beam Propagation Ratios—Part 3: Intrinsic And Geometrical Laser Beam Classification, Propagation And Details of Test Methods," International Organization for Standardization, Geneva, Switzerland, ISO/TR 11146-3:2004/Cor 1:2005, 2005.

[11] *NanoScan V2 Manual.* Ophir-Spiricon, 2015.

[12] G. P. Agrawal, *Fiber-Optic Communication Systems, Third Edition.* New York, United States: John Wiley & Sons, 2002.

[13] L. Borruel, H. Odriozola, J. M. G. Tijero, I. Esquivias, S. Sujecki, and E. C. Larkins, “Design Strategies to Increase the Brightness of Gain Guided Tapered Lasers,” *Optical and Quantum Electronics*, vol. 40, no. 2–4, pp. 175–189, 2008.

[14] L. A. Coldren, S. W. Corzine, and M. L. Mašanovi´c, *Diode Lasers and Photonic Integrated Circuits, Second Edition.* Hoboken, United States: John Wiley & Sons, 2012.

[15] M. W. Davidson, “Metal Oxide Semiconductor (MOS) Capacitor,” http://hamamatsu.magnet.fsu.edu/articles/moscapacitor.html, Accessed: 2018-06-27.

[16] E. Hecht, *Optics, 5th edition.* Pearson Education Limited, 2016, new Jersey, United States.

[17] H. Kogelnik and T. Li, “Laser Beams and Resonators,” *Applied Optics*, vol. 5, no. 10, pp. 1550–1566, 1966.

[18] M. Lehtinen, “High-Brightness Yellow Lasers Set for Breakthroughs in Medicine and Spectroscopy,” http://www.tut.fi/interface/articles/2013/2/high-brightness-yellow-lasers-set-for-breakthroughs-in-medicine-and-spectroscopy, February 2013, Accessed: 2018-06-27.

[19] V. N. Mahajan, *Aberration Theory Made Simple.* Bellingham, United States: SPIE Press, 1991.

[20] G. Morthier and P. Vankwikelberge, *Handbook of Distributed Feedback Laser Diodes.* Norwood, United States: Artech House, Inc., 1997.

[21] J. Niu and J. Xu, “Coupling Efficiency of Laser Beam to Multimode Fiber,” *Optics Communications*, vol. 274, pp. 315–319, 2007.

[22] K. Paschke, S. Einfeldt, A. Ginolas, K. Hausler, P. Ressel, B. Sumpf, H. Wenzel, and G. Erbert, “15-W Reliable Operation of 96-μm Aperture Broad-area Diode Lasers Emitting at 980 nm,” *2008 Conference on Lasers and Electro-Optics and 2008 Conference on Quantum Electronics and Laser Science*, pp. 1–2, 2008.

[23] R. Paschotta, “Beam Parameter Product,” https://www.rp-photonics.com/beam_parameter_product.html, October 2008, Accessed: 2018-06-27.

[24] ——, “Beam Profilers,” https://www.rp-photonics.com/beam_profilers.html, October 2008, Accessed: 2018-06-27.

[25] ——, “Broad Area Laser Diodes,” https://www.rp-photonics.com/broad_area_laser_diodes.html, October 2008, Accessed: 2018-06-27.

[26] ——, “Frequency Doubling,” https://www.rp-photonics.com/frequency_doubling.html, October 2008, Accessed: 2018-06-27.

[27] ——, “Gaussian Beams,” https://www.rp-photonics.com/gaussian_beams.html, October 2008, Accessed: 2018-06-27.

[28] ——, “Optical Pumping,” https://www.rp-photonics.com/optical_pumping.html, October 2008, Accessed: 2018-06-27.

[29] W. Schulz and R. Poprawe, “Manufacturing with Novel High-Power Diode Lasers,” *Journal of Selected Topics in Quantum Electronics*, vol. 6, no. 4, pp. 696–705, 2000.

[30] K. I. Shigihara, K. Kawasaki, Y. Yoshida, S. Yamamura, T. Yagi, and E. Omura, “High-Power 980-nm Ridge Waveguide Laser Diodes Including an Asymmetrically Expanded Optical Field Normal to the Active Layer,” *IEEE Journal of Quantum Electronics*, vol. 38, no. 8, pp. 1081–1088, 2002.

[31] P. Shukla, J. Lawrence, and Y. Zhang, “Understanding Laser Beam Brightness: A Review And New Prospective in Material Processing,” *Optics & Laser Technology*, vol. 75, pp. 40–51, 2015.

[32] A. E. Siegman, *Lasers.* Sausalito, United States: University Science Books, 1986.

[33] ——, “Analysis of Laser Beam Quality Degradation Caused by Quartic Phase Aberrations,” *Applied Optics*, vol. 32, no. 30, pp. 5893–5901, 1993.

[34] ——, “Defining, Measuring, And Optimizing Laser Beam Quality,” *Proceedings of SPIE*, vol. 1868, pp. 2–12, 1993.

[35] ——, “How to (Maybe) Measure Laser Beam Quality,” *OSA Trends in Optics and Photonics*, vol. 17, pp. 184–199, 1998.

[36] G. E. Slobodzian, "Apples to Apples: Which Camera Technologies Work Best for Beam Profiling Applications, Part 4: Scanning Slit vs Camera-Based Beam Analyzers," https://www.ophiropt.com/laser--measurement/knowledge-center/article/8531, Accessed: 2018-06-27.

[37] B. Sumpf, K.-H. Hasler, P. Adamiec, F. Bugge, F. Dittmar, J. Fricke, H. Wenzel, M. Zorn, G. Erbert, and G. Tränkle, "High-Brightness Quantum Well Tapered Lasers," *IEEE Journal of Selected Topics in Quantum Electronics*, vol. 15, no. 3, pp. 1009–1020, 2009.

[38] N. A. Vainos, *Laser Growth and Processing of Photonic Devices.* Cambridge, United Kingdom: Elsevier, 2012.